Study on the Rate-dependent Cyclic Deformation of Super-elastic NiTi Shape Memory Alloy Based on a New Crystal Plasticity Constitutive Model

Chao Yu, Guozheng Kang, Qianhua Kan

PII: S0020-7683(14)00347-3
DOI: http://dx.doi.org/10.1016/j.ijsolstr.2014.09.006
Reference: SAS 8502

To appear in: *International Journal of Solids and Structures*

Received Date: 2 September 2013
Revised Date: 14 April 2014

Please cite this article as: Yu, C., Kang, G., Kan, Q., Study on the Rate-dependent Cyclic Deformation of Super-elastic NiTi Shape Memory Alloy Based on a New Crystal Plasticity Constitutive Model, *International Journal of Solids and Structures* (2014), doi: http://dx.doi.org/10.1016/j.ijsolstr.2014.09.006

Study on the Rate-dependent Cyclic Deformation of Super-elastic NiTi Shape Memory Alloy Based on a New Crystal Plasticity Constitutive Model

Chao Yu[1], Guozheng Kang[*1], Qianhua Kan[2]

[1]State Key Laboratory of Traction Power, Southwest Jiaotong University, Chengdu, Sichuan 610031, P. R. China

[2]School of Mechanics and Engineering, Southwest Jiaotong University, Chengdu, Sichuan 610031, P. R. China

*Correspondent author: Dr. Prof. G.Z. Kang, Tel: 86-28-87603794; Fax: 86-28-87600797

E-mail address: guozhengkang@home.swjtu.edu.cn or guozhengkang@126.com

Abstract

In this paper, a crystal plasticity based constitutive model [Yu, C., Kang, G.Z., Kan, Q.H., Song, D., A micromechanical constitutive model based on crystal plasticity for thermo-mechanical cyclic deformation of NiTi shape memory alloys. Int. J. Plasticity 44 (2013) 161-191] is extended to describe the rate-dependent cyclic deformation of super-elastic NiTi shape memory alloy by considering the internal heat production. Two sources of internal heat productions are included in the proposed model, i.e., the mechanical dissipations of inelastic deformation and the transformation latent heat in the NiTi shape memory alloy. With an assumption of uniform temperature field in the alloy specimen, a simplified evolution law of temperature field is obtained by the first law of thermodynamics and the heat boundary conditions. An explicit scale-transition rule is adopted to extend the proposed single crystal model to the polycrystalline version. The capability of the extended polycrystalline model to describe the rate-dependent cyclic deformation of super-elastic NiTi shape memory alloy is verified by comparing the predictions with the corresponding experimental ones. The comparison demonstrates that the proposed constitutive model considering the internal heat production predicts the rate-dependent cyclic deformation of super-elastic NiTi shape memory alloy fairly well.

Key words: NiTi shape memory alloy; crystal plasticity; cyclic deformation; rate-dependence;

internal heat production.

1. Introduction

NiTi shape memory alloys exhibit unique super-elasticity, shape memory effect and high damping capacity due to their thermo-elastic martensite transformation, and have been widely used in the aeronautic, microelectronic and biomedical industries (Morgan et al., 2004). In services, the structural components made by the NiTi shape memory alloys are often subjected to a cyclic thermo-mechanical loading. The cyclic deformation of the NiTi shape memory alloys is a key issue which should be discussed in advance in order to predict the fatigue life and assess the reliability of such components reasonably and precisely. However, during the cyclic deformation of the NiTi alloys, two features have been observed by many experiments, which must be taken into account in the construction of theoretical model:

- *Transformation ratchetting*: During the cyclic deformation of super-elastic NiTi shape memory alloys, the repeated martensite transformation and its reverse result in a cyclically accumulated residual strain i.e., the transformation ratchetting (Lagoudas and Bo, 1999; Sehitoglu et al., 2001; Nemat-Nasser and Guo, 2006; Zaki and Moumni, 2007a; Kang et al., 2009, 2012; Morin et al., 2011b), and the accumulation rate of residual strain tends to be zero after certain cycles. During the transformation ratchetting deformation, the start stress of the transformation from austenite to martensite phase and the dissipation energy per cycle decrease, but the transformation hardening increases with the number of cycles. The mechanisms of transformation ratchetting are explained by the transformation-induced plasticity occurred at the austenite-martensite interfaces and the accumulation of residual martensite together (Gall and Maier, 2002; Brinson et al. 2004; Kang et al., 2009, 2012). It should be noted that all the experiments mentioned above were preformed actually under the non-isothermal condition due to the internal heat production during the cyclic loading.
- *Rate-dependence*: During the cyclic deformation, the internal heat production of super-elastic NiTi shape memory alloys coming from the mechanical inelastic dissipation and transformation latent heat competes against the heat transfer/convection, and the

transformation stress depends strongly on the test temperature, which leads to a rate-dependent thermo-mechanical cyclic deformation of the NiTi shape memory alloys, as discussed by the existing literature (Shaw, 1995; Grabe and Bruhns, 2008; Christ and Reese, 2009; Zhang et al., 2010; He and Sun, 2010a, 2010b, 2010c, 2011; Morin et al., 2011a, 2011b; Sun et al. 2012; Yin and Sun, 2012; Peigney and Seguin, 2013; Yin et al., 2013, 2014). For example, the additional transformation hardening and the number of macroscopic domains during the martensite transformation increase with the increasing loading rate (Zhang et al., 2010). However, the stress hysteresis varies non-monotonically with the varying loading rate (Zhang et al., 2010; He and Sun, 2010a, 2010b, 2010c, 2011; Morin et al., 2011a, 2011b; Yin et al., 2013,). It should be noted that the rate-dependent cyclic deformation of NiTi shape memory alloys is caused mainly by the internal heat production, which is different from the rate-dependent deformation of ordinary metals caused by the viscosity.

Thus, a theoretical model describing the rate-dependent transformation ratchetting of NiTi shape memory alloys is needed. Based on the experimental results, many constitutive models had been established in the last two decades to describe the thermo-mechanical deformation of NiTi shape memory alloys. The established models can be classified into two groups, i.e., the macro-phenomenological and micromechanical models. The macro-phenomenological models do not concern the complicated microstructures of the NiTi shape memory alloys and their evolutions during the thermo-elastic martensite transformation and its reverse; while they are very suitable for the numerical implementation and then can be easily applied in the structure analysis. The representative models can be referred to those proposed by Bo and Lagoudas (1999a, 1999b, 1999c), Lexcellent et al. (2000), Auricchio et al. (2003, 2007), Lagoudas and Entchev (2004), Lagoudas et al. (2006), Zaki and Moumni (2007a) and Kan and Kang (2010). Recently, Morin et al. (2011b) extended a macroscopic phenomenological thermo-mechanical constitutive model proposed by Zaki and Moumni (2007a) to describe the rate-dependent transformation ratchetting of super-elastic NiTi shape memory alloys by considering the hysteresis dissipation and latent heat simultaneously. The full-coupled governing equations in the proposed model were solved by finite element method (FEM) and rate-dependent transformation ratchetting can be described by the extended model reasonably.

It is well-known that, the macro-phenomenological models can not reasonably reflect the microscopic physical nature of thermo-mechanical deformation of the NiTi shape memory alloys. Thus, in the last decades, many micromechanical constitutive models (Sun and Hwang, 1993a, 1993b; Levitas and Ozsoy, 2009a, 2009b; Levitas 2013; Guthikonda et al., 2013) were developed to describe the super-elasticity and shape memory effect of NiTi shape memory alloys. Among them, the crystal plasticity based constitutive models are popular, since 24 martensite variants with different morphological features and their evolutions during the thermo-mechanical deformation of NiTi shape memory alloys can be reasonably considered in such models. With the help of FEM or homogenization methods such as the self-consistent method and so on, a single crystal model can be extended into a polycrystalline version. Although the crystal plasticity based constitutive model is time-consuming, it is an attractive approach due to its solid physical background. The representative models can be referred to those developed by Patoor et al. (1996, 2006), Huang et al. (1998, 2000), Gall et al. (2000), Gao et al. (2000), Thamburaja and Anand (2001, 2003), Anand and Gurtin (2003), Nae et al. (2003), Thamburaja et al. (2005, 2009), Wang et al. (2008), Manchiraja and Anderson (2010), and Yu et al. (2012, 2014). However, the crystal plasticity based micromechanical constitutive models addressed above cannot describe the transformation ratchetting of super-elastic NiTi shape memory alloys observed by Kang et al. (2009), since the physical mechanisms of transformation ratchetting have not been considered yet in these models.

More recently, Yu et al. (2013) constructed a crystal plasticity based constitutive model to describe the transformation ratchetting of super-elastic NiTi shape memory alloys by introducing 24 friction slip systems at the austenite-martensite interfaces (Lagoudas and Entchev, 2004; Kan and Kang et al., 2010; Kang et al., 2012) and considering the accumulation of residual martensite during the cyclic deformation (Gall and Maier, 2002; Brinson et al., 2004). The predictions agreed with the corresponding experiments well at one specific loading rate. However, the internal heat production in the cyclic deformation of NiTi shape memory alloys was neglected in the proposed model. It means that the crystal plasticity based micromechanical constitutive model proposed by Yu et al. (2013) cannot describe the rate-dependent cyclic deformation of the NiTi shape memory alloys observed by Shaw (1995), He and Sun (2010a, 2010b, 2010c, 2011), Morin et al. (2011a, 2011b), Yin and Sun (2012)

and Yin et al. (2014), in which the rate-dependence of cyclic deformation has been proved to be caused by the internal heat production of the NiTi alloy.

Therefore, in this work, the crystal plasticity based constitutive model proposed by Yu et al. (2013) is extended to describe the rate-dependent cyclic deformation of super-elastic NiTi shape memory alloys. Two sources of internal heat productions (i.e., mechanical inelastic dissipation and transformation latent heat) are considered in the extended model. With the assumption of uniform temperature field in the deformed NiTi alloy specimen (Nae et al., 2003; Zhu and Zhang, 2007; He and Sun, 2010b, 2011; Yin and Sun, 2012; Yin et al. 2014), a simplified evolution law of the temperature field is proposed from the first law of thermodynamics. An explicit scale-transition rule considering the inelastic accommodation of single crystal grains is also employed to obtain the polycrystalline constitutive model from the single crystal version. The extended model is firstly verified by comparing the predictions with the corresponding experiments of polycrystalline NiTi shape memory alloy obtained under the uniaxial cyclic loading conditions and at different strain rates (Morin et al., 2011b). Then, the effects of mechanical dissipation and transformation latent heat on the cyclic deformation of the NiTi alloy are discussed by comparing the predictions with the experiments done by Sun et al. (2012). Finally, the effect of initial texture on the rate-dependent transformation ratchetting and some heterogeneous deformation details of the polycrystalline NiTi alloy in the inter-grain scale are discussed.

2. Outline of original model

As mentioned above, the crystal plasticity based constitutive model proposed by Yu et al. (2013) to describe the transformation ratchetting of super-elastic NiTi shape memory alloys will be extended to describe the rate-dependent cyclic deformation of the NiTi alloys further by considering the internal heat production. Therefore, the original constitutive model (Yu et al., 2013) is first outlined in this section to keep the integrity of the content.

2.1 Definitions of inelastic strain

Based on the hypothesis of small deformation, total strain tensor $\boldsymbol{\varepsilon}$ in a representative

volume element (RVE) of a single crystal can be decomposed into three parts, i.e., the elastic strain tensor $\boldsymbol{\varepsilon}^e$, transformation strain tensor $\boldsymbol{\varepsilon}^{tr}$ and transformation-induced plastic strain tensor $\boldsymbol{\varepsilon}^p$. It yields:

$$\boldsymbol{\varepsilon} = \boldsymbol{\varepsilon}^e + \boldsymbol{\varepsilon}^{in} \tag{1-a}$$

$$\boldsymbol{\varepsilon}^{in} = \boldsymbol{\varepsilon}^{tr} + \boldsymbol{\varepsilon}^p \tag{1-b}$$

where, $\boldsymbol{\varepsilon}^{in}$ is the inelastic strain tensor. It is well-known that there are 24 martensite variants in the stress-induced martensite of NiTi shape memory alloys (Otsuka and Ren, 2005). The strain of each martensite variant can be obtained from its habit plane and transformation direction. Since the transformation ratchetting is caused by the two main mechanisms, i.e., the residual martensite and the transformation-induced plasticity, the volume fraction of α-th martensite variant ξ^α can be divided into two parts: the reversible volume fraction ξ_{re}^α and residual one ξ_{ir}^α. Since the transformation-induced plasticity is caused by the friction slip at the austenite-martensite interfaces, it can be assumed that the direction tensors of α-th friction system and α-th martensite variant are the same and the number of friction systems is equal to that of martensite variants (Yu et al. 2013). Thus, the transformation strain $\boldsymbol{\varepsilon}^{tr}$ and the transformation-induced plastic strain $\boldsymbol{\varepsilon}^p$ can be written as:

$$\boldsymbol{\varepsilon}^{tr} = \boldsymbol{\varepsilon}_{re}^{tr} + \boldsymbol{\varepsilon}_{ir}^{tr} = \sum_{\alpha=1}^{24} \xi_{re}^\alpha g^{tr} \mathbf{P}^\alpha + \sum_{\alpha=1}^{24} \xi_{ir}^\alpha g^{tr} \mathbf{P}^\alpha \tag{2a}$$

$$\boldsymbol{\varepsilon}^p = \sum_{\alpha=1}^{24} \gamma^\alpha \mathbf{P}^\alpha \tag{2b}$$

$$\mathbf{P}^\alpha = \frac{1}{2}(\mathbf{m}^\alpha \otimes \mathbf{n}^\alpha + \mathbf{n}^\alpha \otimes \mathbf{m}^\alpha) \tag{2c}$$

where, $\boldsymbol{\varepsilon}_{re}^{tr}$ is the transformation strain produced by the reversible martensite, $\boldsymbol{\varepsilon}_{ir}^{tr}$ is the transformation strain by the residual martensite. ξ_{re}^α, ξ_{ir}^α and $\mathbf{P}^\alpha$ are the reversible volume fraction, residual volume fraction and orientation tensor of the α-th martensite variant, respectively. g^{tr} is the magnitude of shear deformation caused by the martensite transformation. γ^α is the slippage of the α-th friction slip system. $\mathbf{m}^\alpha$ and $\mathbf{n}^\alpha$ are the

transformation orientation and habit plane normal vectors, respectively. The details for each $\mathbf{m}^{\alpha}$ and $\mathbf{n}^{\alpha}$ can be found in Yu et al. (2013).

2.2 Evolution laws of martensite volume fractions and transformation-induced plasticity

In Section 2.1, it is seen that the internal variables related to the inelastic deformation are the martensite volume fractions ξ_{re}^{α} and ξ_{ir}^{α}, and the slippage γ^{α}, respectively. The driving forces of thermodynamics corresponding to the above-mentioned internal variables are set to be π_{re}^{α}, π_{ir}^{α} and π_{γ}^{α}, respectively, i.e.,

$$\pi_{re}^{\alpha} \leftrightarrow \dot{\xi}_{re}^{\alpha} \tag{3a}$$

$$\pi_{ir}^{\alpha} \leftrightarrow \dot{\xi}_{ir}^{\alpha} \tag{3b}$$

$$\pi_{\gamma}^{\alpha} \leftrightarrow \dot{\gamma}^{\alpha} \tag{3c}$$

It should be noted that, the driving forces of thermodynamics depend on the Helmholtz energy and their explicit forms can be referred to the original work (Yu et al., 2013) or the derivation in Section 3. Here, only the evolution laws of internal variables adopted in the original model are outlined.

For the volume fraction of reversible martensite ξ_{re}^{α}, the Kuhn-Tucker conditions for the forward transformation from austenite to martensite phase and its reverse are written as:
For the forward transformation

$$\dot{\xi}_{re}^{\alpha} \geq 0, \quad \pi_{re}^{\alpha} - Y \leq 0, \quad \dot{\xi}_{re}^{\alpha}(\pi_{re}^{\alpha} - Y) \leq 0 \tag{4a}$$

and for the reverse transformation

$$\dot{\xi}_{re}^{\alpha} \leq 0, \quad \pi_{re}^{\alpha} + Y \geq 0, \quad \dot{\xi}_{re}^{\alpha}(\pi_{re}^{\alpha} + Y) \leq 0 \tag{4b}$$

Where, Y is the transformation resistance which controls the range of elastic unloading (i.e., the width of hysteresis loops) before the reverse transformation from martensite to austenite phase occurs.

When the rate of reversible martensite volume fraction $\dot{\xi}_{re}^{\alpha}$ is non-zero, the consistent conditions as the following should be satisfied, i.e.,

$$\dot{\xi}_{re}^{\alpha}(\dot{\pi}_{re}^{\alpha}-\dot{Y})=0 \quad \text{if} \quad \pi_{re}^{\alpha}-Y=0 \tag{5a}$$

$$\dot{\xi}_{re}^{\alpha}(\dot{\pi}_{re}^{\alpha}+\dot{Y})=0 \quad \text{if} \quad \pi_{re}^{\alpha}+Y=0 \tag{5b}$$

Moreover, all the martensite volume fractions should be constrained within the following ranges:

$$\xi_{ir}^{\alpha}\le\xi^{\alpha}\le 1 \qquad 0\le\xi_{re}^{\alpha}\le 1 \qquad 0\le\xi_{ir}^{\alpha}\le 1 \tag{6a}$$

$$\sum_{\alpha=1}^{24}\xi_{ir}^{\alpha}\le\sum_{\alpha=1}^{24}\xi^{\alpha}\le 1 \qquad 0\le\sum_{\alpha=1}^{24}\xi_{re}^{\alpha}\le 1 \qquad 0\le\sum_{\alpha=1}^{24}\xi_{ir}^{\alpha}\le 1 \tag{6b}$$

It should be noted that, if the constraint equations (i.e., Eqs. (6a) and (6b)) are not satisfied in a certain step of calculation, the $\dot{\xi}_{re}^{\alpha}$ should be set as zero.

For the volume fraction of residual martensite ξ_{ir}^{α}, it can be further decomposed into two parts, i.e., the accumulated one $\xi_{ir,1}^{\alpha}$ and the recovered one $\xi_{ir,2}^{\alpha}$, in order to reflect the observed experimental phenomenon that the residual martensite can be partially recovered in the sequential heating process (Kang et al., 2012). The evolution equation of accumulated residual martensite $\xi_{ir,1}^{\alpha}$ is set as:

$$\dot{\xi}_{ir,1}^{\alpha}=f^{ir}(\xi_{re}^{\alpha},\xi_{ir,1}^{\alpha})\left|\dot{\xi}_{re}^{\alpha}\right|H(\pi_{ir}^{\alpha}) \tag{7}$$

where, f^{ir} is a non-negative function and its mathematical expression can be referred to Yu et al. (2013). The term $H(\pi_{ir}^{\alpha})$ ensures the compatibility of thermodynamics.

The evolution equation of recovered one $\xi_{ir,2}^{\alpha}$ is written as:

$$\dot{\xi}_{ir,2}^{\alpha}=-\left\langle\frac{\dot{T}}{h_T}\right\rangle H(-\pi_{ir}^{\alpha}) \tag{8}$$

where, h_T is the modulus for the thermal recovery of residual martensite. $\langle\bullet\rangle$ is MaCauley bracket: when $x\ge 0$, $\langle x\rangle=x$; when $x<0$, $\langle x\rangle=0$.

Since the transformation-induced plasticity is caused by the irreversible friction slip at the austenite-martensite interfaces, it accumulates during the cyclic deformation and can not be recovered. The evolution equation of slippage γ^{α} is written as:

$$\dot{\gamma}^{\alpha} = f^{p}(\xi_{re}^{\alpha}, \gamma^{\alpha}) \left| \dot{\xi}_{re}^{\alpha} \right| H(\pi_{\gamma}^{\alpha}) \tag{9}$$

where, f^{p} is also a non-negative function and its expression can be referred to Yu et al. (2013). The term $H(\pi_{\gamma}^{\alpha})$ also ensures the compatibility of thermodynamics.

Another important issue in modeling the cyclic thermo-mechanical deformation of NiTi shape memory alloys is how to describe the transformation hardening caused by the martensite transformation and its reverse. To this end, the transformation resistance X^{α} is used and is set as a function of the reversible martensite volume fraction ξ_{re}^{α}, i.e.,

$$X^{\alpha} = H^{\alpha} \xi_{re}^{\alpha} \tag{10}$$

Where, H^{α} is the hardening modulus and its expression is also referred to Yu et al. (2013).

Eqs. (1)~(10) are the framework of the original model, which is proposed to describe the cyclic deformation of NiTi shape memory alloy single crystals without considering the internal heat production.

2.3. Scale-transition rule

To obtain the polycrystalline responses from that of each single crystal grain, a self-consistent scale-transition rule proposed by Berveiller and Zaoui (1979) is referred in this paper. With the same assumption of uniform stress and strain fields in one specified grain, the uniform local stress tensor $\boldsymbol{\sigma}_i$ in the *i*-th grain can be obtained from the applied uniform macroscopic stress tensor $\boldsymbol{\Sigma}$ by using following formulations:

$$\boldsymbol{\sigma}_i = \boldsymbol{\Sigma} + 2\alpha\mu \frac{2(4-5\nu)}{15(1-\nu)} (\mathbf{E}^{in} - \boldsymbol{\varepsilon}_i^{in}) \tag{11-a}$$

$$\mathbf{E}^{in} = \frac{\sum_{i=1}^{n} V_i \boldsymbol{\varepsilon}_i^{in}}{\sum_{i=1}^{n} V_i} \tag{11-b}$$

where, $\boldsymbol{\varepsilon}_i^{in}$ is the inelastic strain tensor in the *i*-th grain. $\mathbf{E}^{in}$ represents the macroscopic inelastic strain tensor of polycrystalline aggregates obtained by the volume average of inelastic strain in each single crystal grain. V_i is the volume fraction of the *i*-th grain. α is a

material parameter and its value should be set to be varied between 0 and 1. When α=1, only the elastic interaction is considered and this model is reduced to the Kröner's model (Kröner 1961); when α=0, the interactions between the grains are neglected and the stress field is uniform in the whole polycrystalline aggregates. The term $2\alpha\mu\frac{2(4-5\nu)}{15(1-\nu)}$ in Eq. (11a) is replaced by a scalar parameter D in this paper for simplicity, i.e., $D=2\alpha\mu\frac{2(4-5\nu)}{15(1-\nu)}$ and the value of D should be set to be within the range from 0 to $2\mu\frac{2(4-5\nu)}{15(1-\nu)}$.

3. Extended model considering internal heat production

As commented in the Introduction, the original constitutive model without considering the internal heat production outlined in Section 2 cannot reasonably describe the rate-dependent cyclic deformation of super-elastic NiTi shape memory alloy, since such rate-dependence is mainly caused by the internal heat production coming from both the mechanical inelastic dissipation and transformation latent heat. Thus, in this section, the original model is extended to describe the rate-dependent cyclic deformation of the NiTi alloy by considering the internal heat production.

In the extended model, the definitions of inelastic strains are the same as that in the original model, i.e., the same as Eqs. (1) and (2). Based on such definitions of inelastic strains, the main equations of extended model are deduced in the following subsections.

3.1 Helmholtz free energy and thermodynamic driving forces

Since the extended model should also satisfy the constraints of thermodynamics, the Helmholtz free energy and corresponding thermodynamic driving forces are first formulated in this section, even if some formulations are the same as that obtained in the original model (Yu et al., 2013) in form. The Helmholtz free energy ψ of the representative volume element (RVE) of single crystal grain is formulated as (Yu et al. 2013):

$$\psi = \psi^{e} + \psi^{\text{int}} + \psi^{ch} + \psi^{tr} \tag{12}$$

where, ψ^{e} is the elastic energy; ψ^{int} is an additional energy caused by the internal stress in the single crystal grain; ψ^{ch} is the chemical energy caused by the difference of entropy between the austenite and martensite phases; ψ^{tr} is the hardening/softening energy caused by the martensite transformation. The explicit expression of each term in the Helmholtz free energy, i.e., Eq. (13), can be written as:

$$\psi^{e}(\boldsymbol{\varepsilon}^{e}) = \frac{1}{2}\boldsymbol{\varepsilon}^{e} : \mathbf{C}(\xi) : \boldsymbol{\varepsilon}^{e} \tag{13a}$$

$$\psi^{ch}(T,\xi) = c[(T - T_0) - T\ln(\frac{T}{T_0})] + \beta(T - T_0)\xi \tag{13b}$$

$$\dot{\psi}^{\text{int}} = -\mathbf{B} : \dot{\boldsymbol{\varepsilon}}^{in} \tag{13c}$$

$$\dot{\psi}^{tr} = \sum_{\alpha=1}^{24} X^{\alpha}\dot{\xi}^{\alpha} \tag{13d}$$

where $\mathbf{C}(\xi)$ is the fourth-ordered elastic modulus tensor, which is dependent on the martensite volume fraction, i.e., $\mathbf{C}(\xi) = (1-\xi)\mathbf{C}_A + \xi\mathbf{C}_M$. $\mathbf{C}_A$ is the elastic modulus tensor of austenite phase and $\mathbf{C}_M$ is the elastic modulus tensor of martensite phase. It implies that, different from the original model (Yu et al., 2013), the extended model addresses the difference of elastic modulus between the austenite and martensite phases and its effect on the cyclic deformation of super-elastic NiTi shape memory alloy. The explicit expression of ψ^{ch} is referred to Lagoudas and Entchev (2004). β is a constant, named as the coefficient of entropy difference between the austenite and martensite phase. T_0 is the balance temperature. c is the heat capacity within a specific volume. X^{α} is the transformation resistance of the α-th martensite variant, which is a power-conjugated variable to $\dot{\xi}^{\alpha}$. $\mathbf{B}$ is the an internal variable called as internal stress tensor and is a power-conjugated variable to $\dot{\boldsymbol{\varepsilon}}^{in}$ and is divided into 24 components as done in the original model, i.e.,

$$\mathbf{B} = \sum_{\alpha=1}^{24} \mathbf{B}^{\alpha} \tag{14}$$

where $\mathbf{B}^{\alpha}$ is the internal stress caused by the α-th martensite variant. Furthermore, it is assumed that the orientation of $\mathbf{B}^{\alpha}$ is the same as that of the corresponding martensite variant. So, the $\mathbf{B}^{\alpha}$ can be written as:

$$\mathbf{B}^{\alpha} = \left\| \mathbf{B}^{\alpha} \right\| \mathbf{P}^{\alpha} \tag{15}$$

where, $\left\| \mathbf{B}^{\alpha} \right\|$ is the norm of $\mathbf{B}^{\alpha}$. More details about the internal stress can be referred to Yu et al. (2013).

The well-known Clausius dissipative inequality is

$$\Gamma = \boldsymbol{\sigma} : \dot{\boldsymbol{\varepsilon}} - \dot{\psi} - \eta \dot{T} - \frac{\mathbf{q} \cdot \nabla T}{T} \geq 0 \tag{16}$$

where, Γ is the total dissipation; T is the ambient temperature; $\mathbf{q}$ is the heat flux vector; and $-\dfrac{\mathbf{q} \cdot \nabla T}{T}$ is the dissipation caused by the heat flux. In the original model (Yu et al., 2013), the term $-\dfrac{\mathbf{q} \cdot \nabla T}{T}$ is neglected, because no thermal effect is considered there.

Substituting Eqs. (1), (2), and (13) into Eq. (16), and considering the Fourier's law of heat flux, i.e.,

$$\mathbf{q} = -\mathbf{k} \cdot \nabla T \tag{17}$$

it yields

$$\begin{aligned} \Gamma = & \underbrace{\left(\boldsymbol{\sigma} - \frac{\partial \psi}{\partial \boldsymbol{\varepsilon}^{e}} \right) : \dot{\boldsymbol{\varepsilon}}^{e}}_{elasticity} + \underbrace{(-\eta - \frac{\partial \psi}{\partial T}) \dot{T}}_{entropy} \\ & \underbrace{+ \sum_{\alpha=1}^{24} [g^{tr}(\boldsymbol{\sigma} + \mathbf{B}) : \mathbf{P}^{\alpha} - \beta(T - T_0) - X^{\alpha} - \frac{1}{2} \boldsymbol{\varepsilon}^{e} : \Delta \mathbf{C} : \boldsymbol{\varepsilon}^{e}] \dot{\xi}_{re}^{\alpha}}_{reversible\ martensite\ dissipation} \\ & \underbrace{+ \sum_{\alpha=1}^{24} [g^{tr}(\boldsymbol{\sigma} + \mathbf{B}) : \mathbf{P}^{\alpha} - \beta(T - T_0) - X^{\alpha} - \frac{1}{2} \boldsymbol{\varepsilon}^{e} : \Delta \mathbf{C} : \boldsymbol{\varepsilon}^{e}] \dot{\xi}_{ir}^{\alpha}}_{residual\ martensite\ disspation} \\ & \underbrace{+ \sum_{\alpha=1}^{24} [(\boldsymbol{\sigma} + \mathbf{B}) : \mathbf{P}^{\alpha}] \dot{\gamma}^{\alpha}}_{plasticity\ disspation} + \underbrace{\frac{\mathbf{k} : (\nabla T \otimes \nabla T)}{T}}_{heat\ flux\ disspation} \geq 0 \end{aligned} \tag{18}$$

where, $\Delta \mathbf{C} = \mathbf{C}_M - \mathbf{C}_A$ is the difference of elastic modulus between the austenite and

martensite phases which is neglected in the original work (Yu et al., 2013). $\mathbf{k}$ is the heat conductivity coefficient, a second-ordered positive definite tensor.

From Eq. (18), the elastic stress-strain relationship, entropy-temperature equation, and relative thermodynamic driving forces can be obtained as:

$$\boldsymbol{\sigma} = \frac{\partial \psi^e}{\partial \boldsymbol{\varepsilon}^e} = \mathbf{C}(\xi) : \boldsymbol{\varepsilon}^e \tag{19a}$$

$$\eta = -\frac{\partial \psi^{ch}}{\partial T} = -\beta\xi + c\ln(\frac{T}{T_0}) \tag{19b}$$

$$\pi_{re}^{\alpha} = g^{tr}(\boldsymbol{\sigma} + \mathbf{B}) : \mathbf{P}^{\alpha} - \beta(T - T_0) - X^{\alpha} - \frac{1}{2}\boldsymbol{\varepsilon}^e : \Delta\mathbf{C} : \boldsymbol{\varepsilon}^e \tag{19c}$$

$$\pi_{ir}^{\alpha} = g^{tr}(\boldsymbol{\sigma} + \mathbf{B}) : \mathbf{P}^{\alpha} - \beta(T - T_0) - X^{\alpha} - \frac{1}{2}\boldsymbol{\varepsilon}^e : \Delta\mathbf{C} : \boldsymbol{\varepsilon}^e \tag{19d}$$

$$\pi_{\gamma}^{\alpha} = (\boldsymbol{\sigma} + \mathbf{B}) : \mathbf{P}^{\alpha} \tag{19e}$$

In the original model (Yu et al., 2013), the dissipation caused by the inelastic deformation is proved to be non-negative, i.e.,

$$\Gamma_{\text{int}} = \sum_{\alpha=1}^{24}(\pi_{re}^{\alpha}\dot{\xi}_{re}^{\alpha} + \pi_{ir}^{\alpha}\dot{\xi}_{ir}^{\alpha} + \pi_{\gamma}^{\alpha}\dot{\gamma}^{\alpha}) \geq 0 \tag{20}$$

Also, it is easily obtained that the heat flux dissipation is non-negative because the tensor $\mathbf{k}$ is positive definite, i.e.,

$$\frac{\mathbf{k} : (\nabla T \otimes \nabla T)}{T} \geq 0 \tag{21}$$

It is seen that the extended model is thermodynamically compatible, if Eqs. (20) and (21) are satisfied; and then can be used to describe the cyclic thermo-mechanical deformation of NiTi shape memory alloys.

3.2 Thermo-mechanical coupling analysis

Generally, the physical fields (such as the displacement, stress, strain and temperature fields) in the whole material domain are the functions of time t and position $\mathbf{x}$, i.e., the displacement $\mathbf{u} = \mathbf{u}(\mathbf{x}, t)$, stress $\boldsymbol{\sigma} = \boldsymbol{\sigma}(\mathbf{x}, t)$, strain $\boldsymbol{\varepsilon} = \boldsymbol{\varepsilon}(\mathbf{x}, t)$, and temperature $T = T(\mathbf{x}, t)$, respectively.

It is well known that, for the RVE of single crystal grain, the first law of thermodynamics can be written as:

$$\dot{U} = \boldsymbol{\sigma} : \dot{\boldsymbol{\varepsilon}} - \nabla \cdot \mathbf{q} \tag{22}$$

where, U and $\mathbf{q}$ is the internal energy and heat flux in the RVE, respectively. Considering the relation between the internal energy and the Helmholtz free energy, i.e.,

$$\psi = U - T\eta \tag{23}$$

Eq. (22) can be rewritten as:

$$\begin{aligned} T\dot{\eta} &= \boldsymbol{\sigma} : \dot{\boldsymbol{\varepsilon}} - \dot{\psi} - \eta\dot{T} - \nabla \cdot \mathbf{q} \\ &= \sum_{\alpha=1}^{24} (\pi_{re}^{\alpha}\dot{\xi}_{re}^{\alpha} + \pi_{ir}^{\alpha}\dot{\xi}_{ir}^{\alpha} + \pi_{\gamma}^{\alpha}\dot{\gamma}^{\alpha}) - \nabla \cdot \mathbf{q} \end{aligned} \tag{24}$$

From Eq. (24), the fully-coupled governing equations for the thermo-mechanical deformation of NiTi shape memory alloys can be deduced as follows:

Substituting Eqs. (17) and (19b) into Eq. (24) yields

$$\begin{aligned} c\frac{\partial T}{\partial t} - \nabla \cdot (\mathbf{k} \cdot \nabla T) = & \underbrace{\sum_{\alpha=1}^{24} \pi_{tr}^{\alpha}(\mathbf{x},t)\dot{\xi}_{re}^{\alpha}(\mathbf{x},t) + \sum_{\alpha=1}^{24} \pi_{tr}^{\alpha}(\mathbf{x},t)\dot{\xi}_{ir}^{\alpha}(\mathbf{x},t) + \sum_{\alpha=1}^{24} \pi_{\gamma}^{\alpha}(\mathbf{x},t)\dot{\gamma}^{\alpha}(\mathbf{x},t)}_{mechanical\ disspation} \\ & + \underbrace{\beta T(\mathbf{x},t)\sum_{\alpha=1}^{24} \dot{\xi}^{\alpha}(\mathbf{x},t)}_{latent\ heat} \end{aligned} \tag{25}$$

Eq. (25) is the heat equilibrium equation in the form of temperature, which should be satisfied during the thermo-mechanical deformation of the NiTi alloys. From Eq. (25), it is seen that the $\sum_{\alpha=1}^{24} \pi_{tr}^{\alpha}\dot{\xi}_{re}^{\alpha}$, $\sum_{\alpha=1}^{24} \pi_{tr}^{\alpha}\dot{\xi}_{ir}^{\alpha}$, and $\sum_{\alpha=1}^{24} \pi_{\gamma}^{\alpha}\dot{\gamma}^{\alpha}$ are the dissipations caused by the martensite transformation, accumulation of residual martensite and friction slip, respectively. All of them are non-negative. $\beta T\sum_{\alpha=1}^{24} \dot{\xi}^{\alpha}$ is the transformation latent heat, and is positive during the forward transformation from austenite to martensite phase but is negative during the reverse transformation from induced martensite to austenite phase.

According to the static equilibrium condition of deformed body, the mechanical equilibrium equation is written as:

$$\nabla \cdot \boldsymbol{\sigma} = \mathbf{0} \tag{26}$$

Eqs. (25) and (26) are the obtained governing equations for the thermo-mechanical deformation of NiTi shape memory alloys. Under specific boundary conditions, the stress and temperature fields in the whole material domain (either the single crystal or polycrystalline materials) can be solved with the help of numerical methods, such as the finite element method (FEM). However, such calculations for the exact solutions of equilibrium equations are very time-consuming (especially for the cyclic deformation of polycrystalline materials). Thus, some simplified methods are needed to solve the above-mentioned equations in order to obtain the thermo-mechanical responses of polycrystalline NiTi shape memory alloys.

3.3 Simplified method to obtain temperature field

Since it is very time-consuming to obtain the temperature field by numerically solving the heat equilibrium equation (Eq.25) with the help of finite element method, some simplified methods are needed. Based on the assumption of uniform temperature field (Nae et al., 2003; Zhu and Zhang, 2007; He and Sun, 2010b, 2011; Yin and Sun, 2012; Yin et al. 2014), a simplified method is proposed to obtain the temperature field from the heat equilibrium equation in this section by referring to the work done by Nae et al. (2003), Zhu and Zhang (2007), He and Sun (2010b, 2011), Yin and Sun, (2012), and Yin et al. (2014):

Considering a polycrystalline material domain Ω, which contains many single crystal grains, and the number of grains is n. The surface of the domain is denoted as S. Integrating Eq. (25) in the whole domain Ω yields

$$c\frac{\partial}{\partial t}\int_{\Omega} T(\mathbf{x},t)dV - \int_{\Omega}\nabla\cdot(\mathbf{k}\cdot\nabla T)dV = \int_{\Omega} g(\mathbf{x},t)dV \tag{27a}$$

$$g(\mathbf{x},t) = \sum_{\alpha=1}^{24}\pi_{tr}^{\alpha}(\mathbf{x},t)\dot{\xi}_{re}^{\alpha}(\mathbf{x},t) + \sum_{\alpha=1}^{24}\pi_{tr}^{\alpha}(\mathbf{x},t)\dot{\xi}_{ir}^{\alpha}(\mathbf{x},t) + \sum_{\alpha=1}^{24}\pi_{\gamma}^{\alpha}(\mathbf{x},t)\dot{\gamma}^{\alpha}(\mathbf{x},t) + \beta T(\mathbf{x},t)\sum_{\alpha=1}^{24}\dot{\xi}^{\alpha}(\mathbf{x},t) \tag{27b}$$

where, $g(\mathbf{x},t)$ is the internal heat source, and V represents the volume of the domain Ω. Then, the overall average temperature and internal heat source in the whole domain Ω can be defined simply as (He and Sun, 2010b, 2011; Yin and Sun, 2012; Yin et al., 2014):

$$T_{av}(t) = \frac{1}{V}\int_{\Omega} T(\mathbf{x},t)dV \tag{28a}$$

$$g_{av}(t)=\frac{1}{V}\int_{\Omega} g(\mathbf{x},t)dV \tag{28b}$$

As a body-centered cubic crystal, the heat conductivity of austenite phase is isotropic. For simplicity, it is further assumed that there is no difference of conductivity coefficients between the austenite and martensite phases of NiTi shape memory alloys. Thus, the second-ordered conductivity coefficient tensor $\mathbf{k}$ can be simplified as:

$$\mathbf{k}=k\mathbf{I} \tag{29}$$

where, k is a scalar constant and $\mathbf{I}$ is the second-ordered unit tensor. Substituting Eqs. (28) and (29) into Eq. (27a) and remembering that the volume integrals can be converted to the surface integrals by using Gauss's theory, it yields,

$$cV\frac{dT_{av}}{dt}=g_{av}V+\oint_S \mathbf{n}\cdot(k\nabla T)dS \tag{30}$$

where, $\mathbf{n}$ is the normal direction in the surface S. Eq. (30) describes the evolution of overall average temperature in the whole polycrystalline material domain. Considering the Newton's boundary condition, i.e.,

$$\mathbf{n}\cdot(k\nabla T)=h(T_r-T_s) \quad \text{on } S \tag{31}$$

where, T_s is the surface temperature on S. T_r is the ambient temperature. h is the heat exchange coefficient of ambient media. It is known that the temperature field in the domain Ω is heterogeneous during the martensite transformation due to the existence of sub-domains and interfaces (Shaw, 1995; Sun and Li, 2002; Zhang et al., 2010). However, the characteristic time of heat conduction is much shorter than the time cost by the martensite transformation. Thus, the heterogeneity of local temperature is a minor factor in determining the global stress-strain responses of NiTi shape memory alloys (He and Sun, 2011). That is, the assumption of uniform temperature field in the whole polycrystalline domain Ω is a reasonable approximation to the temperature field of NiTi shape memory alloys considering the internal heat production, which has been adopted by Nae et al. (2003), Zhu and Zhang (2007), He and Sun (2010b, 2011), Yin and Sun, (2012), and Yin et al. (2014).

By this assumption, the temperature of each material point in the domain Ω and surface S can be considered to be the same as the overall average temperature, i.e.,

$$T = T_s = T_{av} \tag{32}$$

Substituting Eqs. (31) and (32) into Eq. (30) yields

$$c\frac{dT}{dt} = g_{av} + \frac{h(T_r - T)\overline{S}}{V} \tag{33}$$

where, $\overline{S}$ is the total area of the surface S for the domain Ω and can be easily obtained after the geometry of the polycrystalline domain is known. It is seen that with the assumption of uniform temperature field, Eq. (25) is reduced to Eq. (33) when the Newton's boundary condition is considered. It should be noted that although the temperature field is assumed to be uniform here, the heterogeneity of the stress-strain field in the polycrystalline domain can not be neglected. In Section 2.3, an explicit scale-transition rule is adopted to consider the heterogeneous stress-strain field of polycrystalline aggregates. It should be noted that the mechanical equilibrium equation (Eq. (26)) is satisfied automatically in the transition from a single crystal grain to the polycrystalline aggregates by using the mentioned explicit scale-transition rule. It means that Eq. (26) can be simply reduced to Eq. (11). Since the stress, strain and temperature fields are all uniform in one specific single crystal grain of NiTi shape memory alloy, all the internal variables $\dot{\xi}_{re}^{\alpha}$, $\dot{\xi}_{ir}^{\alpha}$, and $\dot{\gamma}^{\alpha}$, and the thermodynamic driving forces π_{re}^{α}, π_{ir}^{α} and π_{γ}^{α} are uniform, too. Consequently, the overall average internal heat source g_{av} in the whole polycrystalline domain Ω can be obtained as follows:

$$g_{av} = \frac{\sum_{i=1}^{n} V_i \left(\sum_{\alpha=1}^{24} \pi_{tr}^{\alpha} \dot{\xi}_{re}^{\alpha} + \sum_{\alpha=1}^{24} \pi_{tr}^{\alpha} \dot{\xi}_{ir}^{\alpha} + \sum_{\alpha=1}^{24} \pi_{\gamma}^{\alpha} \dot{\gamma}^{\alpha} + \beta T \sum_{\alpha=1}^{24} \dot{\xi}^{\alpha}\right)_i}{\sum_{i=1}^{n} V_i} \tag{34}$$

where, i represents the i-th single crystal grain; V_i is the volume of the i-th grain; n is the total number of grains.

3.4 New evolution equations of X^{α}, Y, $\left\|\mathbf{B}^{\alpha}\right\|$, $\dot{\xi}_{re}^{\alpha}$, $\dot{\xi}_{ir}^{\alpha}$ and $\dot{\gamma}^{\alpha}$

The evolution equations of internal variables X^{α}, Y, $\left\|\mathbf{B}^{\alpha}\right\|$, $\dot{\xi}_{ir}^{\alpha}$ and $\dot{\gamma}^{\alpha}$ are obtained from the corresponding experimental observations. In the next section, the extended model

will be verified by predicting the experimental results obtained by Morin et al. (2011b). During the cyclic deformation, the start stress of martensite transformation and the dissipation energy per cycle decrease, but the transformation hardening increases with the number of cycles. These phenomena tend to be saturated after certain cycles and are similar to that observed by Kang et al. (2009). Thus, the evolution equations of X^{α} (controlling the transformation hardening of the NiTi alloy in an isothermal case), $\|\mathbf{B}^{\alpha}\|$ (controlling the decreasing start stress of martensite transformation) are set as the same as those proposed in the original model (Yu et al. 2013). The explicit expression of X^{α} is given by Eq. (10). The transformation hardening modulus H^{α} in Eq. (10) and the internal stress variable $\|\mathbf{B}^{\alpha}\|$ are given, respectively, as:

$$H^{\alpha} = H_0^{\alpha} + (H_{sat}^{\alpha} - H_0^{\alpha})(1 - \exp(-\frac{\xi_c^{\alpha}}{b_1})) \tag{35-a}$$

$$\|\mathbf{B}^{\alpha}\| = B_{sat}^{\alpha}(1 - \exp(-\frac{\xi_c^{\alpha}}{b_1})) \tag{35-b}$$

$$\dot{\xi}_c^{\alpha} = \left|\dot{\xi}_{re}^{\alpha}\right| \tag{35-c}$$

where, H_0^{α} and H_{sat}^{α} are the initial and saturated values of H^{α}, respectively. B_{sat}^{α} is the saturated value of internal stress. b_1 is a material parameter governing the rate of saturation. ξ_c^{α} is the accumulated volume fraction of the α-th martensite variant.

The variable Y controls the width of hysteresis loop (more details can be found in Section 4.1). It can be deduced from the experimental observation by Morin et al. (2011b) that the range of elastic unloading decreases with the increasing number of cycles and tends to be saturated after certain cycles. So, Y is set as an exponential form which is different from that used in the original model (Yu et al., 2013), i.e.,

$$Y = Y_0 + (Y_{sat} - Y_0)(1 - \exp(-\frac{\sum_{\alpha=1}^{24} \xi_c^{\alpha}}{b_2})) \tag{36}$$

where, Y_0 and Y_{sat} are the initial and saturated values of Y, respectively. The parameter b_2 governs the rate of evolution.

Furthermore, it is shown (Morin et al., 2011b) that at each loading rate, both the peak and residual strains of NiTi shape memory alloy progressively accumulate with the increasing number of cycles, and the residual strain evolutes quicker than the peak strain, which are similar to those observed by Kang et al. (2009). Thus, as discussed in Kang et al. (2009), the accumulated peak and residual strains observed by Morin et al. (2011b) at different loading rates are also caused by both the accumulated residual martensite and transformation-induced plasticity occurred during the cyclic transformation. However, since the peak stresses at various loading rates are set to be the same as that observed in the experiments of Morin et al. (2011b), the dependence of transformation ratchetting on the applied peak stress can be neglected in the extended model. Although the residual martensite is decomposed into two parts, i.e., an accumulated one and a recovered one as shown in Eq. (6) in the previous work (Yu et al., 2013), the partial recovery of residual martensite is neglected here, since the maximum temperature caused by the internal heat production and observed in the experiments of Morin et al. (2011b) is lower than 335K, at which the residual martensite can not easily transform to the austenite phase. Thus, Newly simplified evolution equations of accumulated residual martensite and transformation-induced plasticity are proposed here in the exponential forms, i.e.,

For the accumulated residual martensite:

$$f^{ir} = \frac{\xi_{sat}}{b_1}\exp(-\frac{\bar{\xi}_{c1}^{\alpha}}{b_1}) \tag{37a}$$

$$\dot{\bar{\xi}}_{c1}^{\alpha} = \left|\dot{\xi}_{re}^{\alpha}\right| H(\pi_{ir}^{\alpha}) \tag{37b}$$

For the transformation-induced plasticity:

$$f^{p} = \frac{\gamma_{sat}}{b_1}\exp(-\frac{\bar{\xi}_{c2}^{\alpha}}{b_1}) \tag{38a}$$

$$\dot{\bar{\xi}}_{c2}^{\alpha} = \left|\dot{\xi}_{re}^{\alpha}\right| H(\pi_{\gamma}^{\alpha}) \tag{38b}$$

where, ξ_{sat} and γ_{sat} is the saturation value of ξ_{ir}^{α} and γ^{α}, respectively.

To describe the rate-dependent and rate-independent inelastic deformation in an identical approach, the evolution equation of internal variable ξ_{re}^{α}, i.e., the reversible martensite

volume fraction is set as a rate-dependent power-law form (Eq.39a), rather than the rate-independent form (i.e., Eqs. 4 and 5), because the rate-independent response can be described by the rate-dependent equation with the coefficient m high enough (e.g., m=100).

$$\dot{\xi}_{re}^{\alpha}=\left|\frac{\pi_{re}^{\alpha}}{Y}\right|^{m}\operatorname{sign}(\pi_{re}^{\alpha}) \quad \text{whenever} \quad \xi_{re}^{\alpha}>0 \quad \sum_{\alpha=1}^{24}(\xi_{re}^{\alpha}+\xi_{ir}^{\alpha})<1 \tag{39a}$$

$$\dot{\xi}_{re}^{\alpha}=0 \quad \text{other conditions} \tag{39b}$$

Under the isothermal condition, m represents the rate sensitivity of the martensite transformation. Although the evolution equations of $\dot{\xi}_{re}^{\alpha}$, $\dot{\xi}_{ir}^{\alpha}$ and $\dot{\gamma}^{\alpha}$ are different from those used in the previous work (Yu et al., 2013), they still satisfy the constraints of thermodynamics (Eq. 20). Some necessary proofs are outlined as follows:

For the reversible martensite transformation, by considering Eq. (39), the dissipation caused by the reversible part of the α-th martensite variant can be written as:

$$\pi_{re}^{\alpha}\dot{\xi}_{re}^{\alpha}=0 \quad \text{when} \quad \dot{\xi}_{re}^{\alpha}=0 \tag{40a}$$

$$\pi_{re}^{\alpha}\dot{\xi}_{re}^{\alpha}=\frac{\left|\pi_{re}^{\alpha}\right|^{m+1}}{|Y|^{m}}\geq 0 \quad \text{when} \quad \dot{\xi}_{re}^{\alpha}\neq 0 \tag{40b}$$

From Eqs. (40a) and (40b), it has been proved that $\pi_{re}^{\alpha}\dot{\xi}_{re}^{\alpha}\geq 0$.

For the accumulation of residual martensite, by considering Eq. (37), the dissipation caused by the residual part of the α-th martensite variant can be written as:

$$\pi_{ir}^{\alpha}\dot{\xi}_{ir}^{\alpha}=\frac{\xi_{sat}}{b_1}\exp(-\frac{\bar{\xi}_{c1}^{\alpha}}{b_1})\left|\dot{\xi}_{re}^{\alpha}\right|\left\langle\pi_{ir}^{\alpha}\right\rangle\geq 0 \tag{41}$$

and it is seen that $\pi_{ir}^{\alpha}\dot{\xi}_{ir}^{\alpha}\geq 0$.

For the transformation-induced plasticity, by considering Eq. (38), the dissipation caused by the movement of the α-th friction slip system can be written as:

$$\pi_{\gamma}^{\alpha}\dot{\gamma}^{\alpha}=\frac{\gamma_{sat}}{b_1}\exp(-\frac{\bar{\xi}_{c2}^{\alpha}}{b_1})\left|\dot{\xi}_{re}^{\alpha}\right|\left\langle\pi_{\gamma}^{\alpha}\right\rangle\geq 0 \tag{42}$$

From Eqs. (40) to (42), it is seen that $\pi_{re}^{\alpha}\dot{\xi}_{re}^{\alpha}\geq 0$, $\pi_{ir}^{\alpha}\dot{\xi}_{ir}^{\alpha}\geq 0$ and $\pi_{\gamma}^{\alpha}\dot{\gamma}^{\alpha}\geq 0$. Thus, the constraints of thermodynamics are also satisfied during the evolution of internal variables.

4. Model Verification

4.1 Determination of material parameters

The physical constants used in the proposed model, i.e., c, h and v can be obtained from the references. As mentioned in Section 2.3, the value of parameter D should be set to be in the range from 0 to $2\mu\frac{2(4-5v)}{15(1-v)}$, and then D=3GPa is used in this paper. The other parameters can be obtained by the cyclic stress-strain curves at a specific loading rate and at one temperature, and a tensile stress-strain curve at the other temperature.

Fig. 1a shows the cyclic stress-strain curves (at the temperature T_1) and the partial stress-strain curve (at the temperature T_2) of the polycrystalline NiTi shape memory alloy obtained at a specific strain rate. The blue solid curve shows the stress-strain curve in the first cycle and the dash curve shows the one in the steady-state cycle at the temperature T_1. The red dash-dot curve shows the partial stress-strain curve in the first cycle at the temperature T_2 and it is noted that $T_2>T_1>A_f$. At the temperature T_1, the start stresses of martensite transformation in the first and steady-state cycles are denoted as σ_{AM}^{0} and σ_{AM}^{sat}, respectively. The residual strain is denoted as ε_r and the transformation strain in the first cycle is denoted as ε_{tr}, respectively. The width of the hysteresis loop in the first and steady-state cycles are W^0 and W^{sat}, respectively. The increment of the peak strain is denoted as $\Delta\varepsilon_{peak}$. At the temperature T_2, the start stresses of martensite transformation in the first cycle is denoted as σ'^{0}_{AM}.

The elastic modulus of the austenite (E_A) and martensite phases (E_M) can be easily obtained from the stress-strain curves as shown in Fig.1. The parameter g^{tr} controls the maximum transformation strain of the NiTi alloy, and then can be obtained from the measured value of ε_{tr}. During the cyclic tension-unloading deformation, the increased peak strain is mainly caused by the transformation-induced plasticity and the increased residual strain is caused by both the transformation-induced plasticity and residual martensite. Thus, the parameters γ_{sat} and ξ_{sat} can be obtained from the measured results of $\Delta\varepsilon_{peak}$ and

$\varepsilon_r - \Delta\varepsilon_{peak}$, respectively.

It is noted that in order to obtain the other material parameters easily, a new parameter called as the reference temperature is introduced here and it can be expressed by other parameters, i.e.,

$$T_{ref} = T_0 - \frac{Y}{\beta} \tag{43}$$

Thus the driving forces of π_{re}^{α} and π_{ir}^{α} (i.e., Eqs. (19b) and (19c)) can be rewritten as:

$$\pi_{re}^{\alpha} = \pi_{ir}^{\alpha} = g^{tr}(\boldsymbol{\sigma} + \mathbf{B}) : \mathbf{P}^{\alpha} - \beta(T - T_{ref}) - X^{\alpha} - \frac{1}{2}\boldsymbol{\varepsilon}^{e} : \Delta\mathbf{C} : \boldsymbol{\varepsilon}^{e} + Y \tag{44}$$

From Eq. (44), it is assumed that in the scale of single crystal grain, the start stress of martensite transformation and its reverse and the finish stress of transformation are $\boldsymbol{\sigma}_1^0$, $\boldsymbol{\sigma}_2^0$ and $\boldsymbol{\sigma}_3^0$ (in the first cycle) for the α-th variant at the temperature T_1, respectively. The start stress of martensite transformation is $\boldsymbol{\sigma}_4^0$ at the temperature T_2.

Noted that the value of the internal stress tensor $\mathbf{B}$ and the transformation resistance X^{α} are all zero when the forward transformation occurs in the first loading cycle. Thus, the conditions for the forward transformation at the temperatures T_1 and T_2 can be written, respectively, as:

$$g^{tr}\boldsymbol{\sigma}_1^0 : \mathbf{P}^{\alpha} - \beta(T_1 - T_{ref}) - \frac{1}{2}\boldsymbol{\sigma}_1^0 : \Delta\mathbf{S} : \boldsymbol{\sigma}_1^0 = 0 \qquad \text{at } T_1 \tag{45a}$$

$$g^{tr}\boldsymbol{\sigma}_4^0 : \mathbf{P}^{\alpha} - \beta(T_2 - T_{ref}) - \frac{1}{2}\boldsymbol{\sigma}_4^0 : \Delta\mathbf{S} : \boldsymbol{\sigma}_4^0 = 0 \qquad \text{at } T_2 \tag{45b}$$

where, $\Delta\mathbf{S} = \mathbf{C}_A^{-1} : \Delta\mathbf{C} : \mathbf{C}_A^{-1}$, $\mathbf{C}_A^{-1}$ is the inverse tensor of $\mathbf{C}_A$. Then, the two parameters β and T_{ref} can be obtained by solving Eqs. (45-a) and (45-b), i.e.,

$$T_{ref} = \frac{T_1(g^{tr}\boldsymbol{\sigma}_4^0 : \mathbf{P}^{\alpha} - \frac{1}{2}\boldsymbol{\sigma}_4^0 : \Delta\mathbf{S} : \boldsymbol{\sigma}_4^0) - T_2(g^{tr}\boldsymbol{\sigma}_1^0 : \mathbf{P}^{\alpha} - \frac{1}{2}\boldsymbol{\sigma}_1^0 : \Delta\mathbf{S} : \boldsymbol{\sigma}_1^0)}{g^{tr}\boldsymbol{\sigma}_4^0 : \mathbf{P}^{\alpha} - \frac{1}{2}\ \boldsymbol{\sigma}_4^0 : \Delta\mathbf{S} : \boldsymbol{\sigma}_4^0 - g^{tr}\boldsymbol{\sigma}_1^0 : \mathbf{P}_{tr}^{\alpha} + \frac{1}{2}\boldsymbol{\sigma}_1^0 : \Delta\mathbf{S} : \boldsymbol{\sigma}_1^0} \tag{46a}$$

$$\beta = \frac{g^{tr}\boldsymbol{\sigma}_4^0 : \mathbf{P}^{\alpha} - \frac{1}{2}\boldsymbol{\sigma}_4^0 : \Delta\mathbf{S} : \boldsymbol{\sigma}_4^0 - g^{tr}\boldsymbol{\sigma}_1^0 : \mathbf{P}^{\alpha} + \frac{1}{2}\boldsymbol{\sigma}_1^0 : \Delta\mathbf{S} : \boldsymbol{\sigma}_1^0}{T_2 - T_1} \tag{46b}$$

It is seen that β and T_{ref} are the functions of $\boldsymbol{\sigma}_1^0$ and $\boldsymbol{\sigma}_4^0$. For the polycrystalline NiTi

shape memory alloy (under the uniaxial loading condition), β and T_{ref} can be obtained from the measured start stresses of martensite transformation in the first cycle at the temperature T_1 and T_2 (i.e., σ_{AM}^0 and σ'^0_{AM}). By Eq. (44), the finish point of martensite transformation and the start point of its reverse in the first cycle can be written as:

$$g^{tr}\boldsymbol{\sigma}_2^0 : \mathbf{P}^{\alpha} - \beta(T_1 - T_{ref}) - X^{\alpha} - \frac{1}{2}\boldsymbol{\sigma}_2^0 : \Delta\mathbf{S} : \boldsymbol{\sigma}_2^0 = 0 \tag{47a}$$

$$g^{tr}\boldsymbol{\sigma}_3^0 : \mathbf{P}^{\alpha} - \beta(T_1 - T_{ref}) - X^{\alpha} - \frac{1}{2}\boldsymbol{\sigma}_3^0 : \Delta\mathbf{S} : \boldsymbol{\sigma}_3^0 = -2Y_0 \tag{47b}$$

Then, it yields

$$Y_0 = \frac{g^{tr}}{2}(\boldsymbol{\sigma}_2^0 - \boldsymbol{\sigma}_3^0) : \mathbf{P}^{\alpha} + \frac{1}{4}\boldsymbol{\sigma}_3^0 : \Delta\mathbf{S} : \boldsymbol{\sigma}_3^0 - \frac{1}{4}\boldsymbol{\sigma}_2^0 : \Delta\mathbf{S} : \boldsymbol{\sigma}_2^0 \tag{48}$$

Thus, the variable Y_0 controls the width of the hysteresis loop in the first cycle. For the polycrystalline NiTi shape memory alloy (under uniaxial loading condition) it can be obtained from the measured values of W^0. Similarly, the variable Y_{sat} controls the width of the hysteresis loop in the first cycle and can be obtained from the measured values of W^{sat}. H control the transformation modulus. H_0 and H_{sat} can be obtained from the measured values of h_0 and h_{sat}, respectively. The parameter B_{sat} controls the decreased start stress of the forward transformation, and can be obtained from the difference between the start stresses of martensite transformation in the first and steady-state cycles, i.e., $\sigma_{AM}^0 - \sigma_{AM}^{sat}$. The other parameters b_1 and b_2 controlling the saturated rates of γ and can be obtained by fitting the evolution curves of γ and Y during the cyclic deformation, respectively.

4.2 Simulations of the rate-dependent transformation ratchetting

In this section, the proposed model is used to simulate the uniaxial transformation ratchetting of polycrystalline NiTi shape memory alloy obtained by Morin et al. (2011b) at different strain rates. The critical temperature parameters of polycrystalline NiTi shape memory alloy are: the martensite transformation start temperature M_s =296K and finish

temperature M_f =286K; the austenite transformation start temperature A_s=280K and finish temperature A_f =297K. The ambient temperature is 323K in the experiment of Morin et al. (2011b), and then the original phase of the alloy before testing is the austenite phase. The number of cycles for each loading condition is set as 40. All the tests are performed under the strain-controlled cyclic loading conditions, but the loading ranges are limited by the prescribed stresses. The maximum and minimum stresses for each cycle are set as 800 MPa and 0 MPa, respectively. The tested specimen is a super-elastic wire with a diameter of 2 mm and a length of 100 mm. Thus, the volume and surface area of this polycrystalline specimen are 314.16 mm^3 and 628.32 mm^2, respectively. The explicit scale-transition rule discussed in Section 2.3 is employed to obtain the mechanical responses of polycrystalline aggregates. It should be noted that, most of NiTi shape memory alloy bars and wires exhibit asymmetrical tension-compression responses due to the [111]-type initial texture (Gall and Sehitoglu 1999; Thamburaja and Anand 2001). The martensite transformation start stress of the textured polycrystalline NiTi shape memory alloy presented in the tension is much lower than that in the compression (Gall and Sehitoglu 1999; Thamburaja and Anand 2001). The [111]-type initial texture has been addressed by Yu et al. (2013) to describe the asymmetrical uniaxial transformation ratchetting of super-elastic NiTi shape memory alloy. However, in the experiments done by Morin et al. (2011b), only a repeated tension-unloading test was performed and the asymmetrical tensile-compressive responses could not be observed. Thus, the initial texture of polycrystalline NiTi shape memory alloy wire is neglected in this section with regard to the experimental data by Morin et al. (2011b), and only 40 random single crystal grains are used to represent the polycrystalline aggregates. In Section 5.2, the effect of the [111]-type initial texture on the rate-dependent cyclic deformation of the NiTi shape memory alloy will be discussed.

As mentioned in section 4.1, D is set as 3GPa; the physical constants c, h and v are obtained by referring to Morin et al. (2011b); and other parameters (except for β and T_{ref}) are determined by the cyclic strain-stress curves obtained at the strain rate of 1×10^{-4}/s. Since the experiments were performed by Morin et al. (2011b) only at one specific temperature, i.e., at 323K, the parameters β and T_{ref} cannot be determined by the procedure mentioned in

Section 4.1 due to the lack of the tensile stress-strain curve at the other temperatures. They are obtained only from the start stress of martensite transformation at the strain rate of 1×10^{-4}/s and the hardening modulus of the stress-strain curves (in the first cycle) at the stain rate of 5×10^{-3}/s by the trial-and-error method. All the material parameters are listed in Table 1.

Figs. 2a to 2f show the experimental and simulated stress-strain curves in the first cycle and at six kinds of strain rates, i.e., 1×10^{-4}/s, 2.5×10^{-4}/s, 5×10^{-4}/s, 1×10^{-3}/s, 2.5×10^{-3}/s and 5×10^{-3}/s. The dash lines represent the simulations considering the internal heat production; while the dash-dot lines show the ones without the internal heat production. It is seen that, no transformation hardening is observed when the strain rate is low (e.g., 1×10^{-4}/s). Additional transformation hardening occurs when the strain rate reaches to 1×10^{-3}/s as shown in Fig. 1d, and becomes more and more remarkable with the increasing strain rate. The rate-dependent transformation hardening can be captured by the proposed model reasonably. The simulated stress-strain curves are in good agreement with the experimental ones at lower strain rates (i.e., 1×10^{-4}/s~1×10^{-3}/s). However, at relatively higher strain rates (i.e., 2.5×10^{-3}/s and 5×10^{-3}/s), the discrepancies between the experimental and predicted transformation hardening become to be apparent, which is similar to that predicted by the extended Z-M model (Morin et al. 2011b). In fact, the transformation hardening of NiTi shape memory alloy depends on the temperature. However, from Eq. (35a), it is seen that the effect of temperature on the transformation hardening modulus is not considered due to the lack of the experimental stress-strain curves at different temperatures. The hardening modulus used in the proposed model can be improved after more systematic experimental data are obtained. From the dash-dot lines shown in Figs. 2a to 2f, it is seen that if the internal heat production is neglected, the stress-strain curves obtained at various strain rates are almost overlapped. It implies that the viscosity caused by the power-law flow rule (i.e., Eq. (39a)) can be neglected and the rate-dependent transformation ratchetting of the NiTi shape memory alloy is mainly caused by the internal heat production addressed in the proposed model.

Fig. 3a shows the experimental and simulated results of dissipated energy in the first cycle and obtained at different strain rates. It is seen that the stress-strain hysteresis loop varies non-monotonically at different strain rates, which is similar to that reported by He and Sun (2010a, 2010b, 2010c, 2012) and Zhang et al. (2010). The proposed model in this work

describes this phenomenon reasonably. Fig. 3b shows the relationships of the maximum and minimum uniform temperatures vs. strain rate, and it is seen that the predicted results agree with the experimental ones well at low and moderate strain rates. The decrease in the prediction accuracy of the proposed model at higher strain rates (e.g., 2.5×10^{-3}/s and 5×10^{-3}/s) can be explained by the following two reasons: (1) a nonlinear relationship between the start stress of martensite transformation and the temperature was recently observed by Zaki and Moumni (2007b), which means that the parameter β in the proposed model should be dependent on the temperature. However, the parameter β is set as a constant in this paper for simplicity due to the lack of the experimental stress-strain curves at different temperatures. (2) the localization phenomenon (e.g., the temperature in the front of martensite domain is much higher than that in other regions during the transformation) becomes more and more obvious with the increasing strain rate (Morin et al. 2011b), and the heterogeneity of temperature field is not considered here. From Figs. 3a and 3b, it is seen that the predicted dissipated energy and temperatures obtained at various strain rates are almost the same, respectively, if the internal heat production is not included.

Figs. 4a to 4f show the experimental and simulated stress-strain curves in the 10^{th} cycle and at different strain rates. It is seen that both the residual and peak strains increase, but the increase of residual strain is quicker than the peak one. It should be noted that the residual stain is caused by the residual martensite and transformation-induced plasticity together; while the increased peak strain is caused only by the transformation-induced plasticity. The predicted results are in good agreement with the experimental ones.

Figs. 5a and 5b show the experimental and predicted results of dissipated energy and maximum/minimum uniform temperatures in the 10^{th} cycle and at different strain rates, respectively. Both the dissipated energy and maximum/minimum uniform temperatures are reasonably predicted by the proposed model.

Figs. 6a to 6f show the experimental and simulated stress-strain curves in the 40^{th} (stabilized) cycle and at different strain rates. It is seen that the saturation values of peak and residual strains at different strain rates are almost the same. Figs. 7a and 7b show the experimental and predicted results of dissipated energy and maximum/minimum uniform temperatures in the 40^{th} (stabilized) cycle and at different strain rates, respectively. It is seen

that the predicted results are in good agreement with the experimental ones.

5. Discussions

5.1 Effect of mechanical dissipation and transformation latent heat

In the proposed model, two internal heat production mechanisms are considered, i.e., the mechanical dissipation (MD) and transformation latent heat (LH). In this section, in order to distinguish the effects of two internal heat mechanisms on the cyclic deformation of NiTi shape memory alloy, the proposed model is used to simulate and predict the experimental results observed by Sun et al. (2012). The specimens used are super-elastic NiTi wires with 40 mm gauge length and 3.5 mm cross-section diameter. In order to avoid the effect of transformation ratchetting, all the specimens are trained till the shakedown of transformation occurs, before the practical cyclic deformation tests start. Three kinds of loading frequencies are prescribed, i.e., 0.0007Hz, 0.04Hz and 1Hz. The test temperature is set as 298K.

Also, 40 random single crystal grains are used to represent the polycrystalline NiTi shape memory alloy as the same as that in Section 4.2. The physical constants c and h are obtained by referring to Yin and Sun (2012). v and D are set as the same as that listed in Table 1. It is noted that the material parameters related to the transformation ratchetting can be neglected, because the transformation ratchetting was restrained by the training process, i.e., $B_{sat}=0$, $Y_{sat}=Y_0$, $H_{sat}=H_0$, $\gamma_{sat}=0$ and $\xi_{sat}=0$. The parameters E_A, E_M, g^{tr}, Y_0 and H_0 are obtained from the strain-stress curves in the first cycle and at the loading frequency of 0.0007Hz as mentioned in Section 4.1. Similar to Section 4.2, the parameters β and T_{ref} are determined from the start stress of martensite transformation at the loading frequency of 0.0007Hz and the hardening modulus in the first cycle and at the loading frequency of 0.04Hz, respectively, by the trial-and-error method. All the material parameters are listed in Table 2.

Fig. 8a shows the experimental and simulated stress-strain curves of the NiTi shape memory alloy in the first cycle and at the frequency of 0.0007Hz. The solid lines in the figure represent the experiments, and the dash lines show the simulations considering both the transformation latent heat (LH) and mechanical dissipation (MD); while the dash-dot or

dash-dot-dot lines show the predictions considering only the transformation latent heat (LH) or mechanical dissipation (MD), respectively. Fig. 8b gives the corresponding stress-strain curves obtained in the cycle where a steady state of cyclic deformation is reached (i.e., the 3rd cycle). Comparing Figs. 8a and 8b, it is seen that almost no difference exists between the stress-strain responses in the first cycle and steady one. In fact, the heat transfer via the convection and conduction is much faster than the heat production in the loading case at the frequency of 0.0007Hz (Sun et al, 2012; Yin et al., 2014). Thus, the effect of thermal variation on the cyclic deformation of the NiTi shape memory alloy is quite weak. As shown in Figs. 8a and 8b, it implies that the simulations considering both the LH and MD (LH+MD), only the LH and only the MD are the same, and all of them describe the experimental stress-strain curves reasonably. Figs. 9a shows the experimental and simulated evolution curves of the measured temperature. The oscillation of the temperature (self-heating caused by latent heat in loading and self-cooling in unloading. Yin et al. 2014) with a small amplitude is observed and its mean value is the same as the ambient temperature. Fig. 9b and 9c shows the simulated results of the temperature obtained at the loading frequency of 0.0007Hz and by considering the LH+MD, only the LH and only the MD, respectively. It is seen that the simulations considering the LH+MD and only the LH are the same, although the oscillation of the temperature predicted by the proposed model is lower than the experimental ones. However, the oscillation of the temperature cannot be reflected by the simulations considering only the MD. It means the oscillation of the temperature is mainly controlled by the transformation latent heat (LH), rather than the mechanical dissipation (MD).

At the intermediate frequency of 0.04Hz, the combined effect of heat production and heat transfer on the thermo-mechanical responses of NiTi shape memory alloy becomes significant due to the time of heat production is comparable to that of heat transfer (Yin et al. 2014). From Figs. 10 and 11, it is seen that the transformation hardening and the oscillation amplitude of measured temperature are much stronger than that at the frequency of 0.0007Hz. With the decrease of mean temperature, the stress-strain curve moves downward during the cyclic loading. Also, only a slight difference is observed between the simulations considering the LH+MD and only the LH, and both of them agree with the experimental ones fairly well. Similarly, the oscillation of the temperature cannot be reflected by the simulations considering

only the MD. The predicted temperature increases monotonically in the first beginning of cyclic loading due to the non-negativity of the MD and tends to be saturated after five cycles. It implies that the mean temperature in each cycle is controlled by both the transformation latent heat (LH) and mechanical dissipation (MD) at the intermediate frequency.

When the frequency of cyclic deformation reaches to 1Hz, the thermal effect of NiTi shape memory alloy becomes much more significant (as shown in Figs. 12 and 13). The release/absorption of transformation latent heat results in the oscillation of measured temperature. On the other hand, the heat production from the MD cannot be conducted out of the specimen due to the high loading frequency, and then accumulates rapidly in the inner of the specimen, which results in a large increase of mean temperature (Sun et al., 2012; Yin et al., 2014). From Figs. 12 and 13, it is seen that the transformation hardening is very strong and the stress-strain curves shift upward gradually due to the increasing mean temperature. The simulations considering both the LH and MD are in good agreement with the corresponding experimental data; while the simulations considering only the LH or MD differ from the experimental results obviously. Furthermore, from Figs. 13b and 13c, it is seen that the mean temperature in each cycle is mainly controlled by the MD at the high frequency.

It should be noted that a pre-stress of 50MPa is set in the tests for each loading case, and then the start points of recorded experimental and predicted stress-strain curves are not located at the origin point (0, 0), as shown in Figs. 8, 10 and 12.

5.2 Effect of initial texture

As mentioned in Section 4.2, most of the NiTi shape memory alloy bars and wires exhibit asymmetrical tension-compression responses due to the [111]-type initial texture (Gall and Sehitoglu 1999; Thamburaja and Anand 2001). The effect of initial texture on the rate-dependent cyclic deformation which is not considered in Section 4.2 will be discussed in this section. As the same as Section 4.2, 40 single crystal grains are employed to represent the polycrystalline aggregates. To model the [111]-type texture in the polycrystalline NiTi alloy bars and wires, each grain is assigned a specific orientation which makes the [111] directions of all grains being located in a band scattered from 0 to15° regarding to the loading direction. The model parameters are set as the same as those listed in Table 1.

Fig. 14a shows the tension-unloading and compression-unloading stress-strain curves obtained in the 1st and 40th cycle and at strain rate 1×10^{-4}/s for the un-textured polycrystalline aggregates (i.e., 40 random single crystal grains). It is seen that the two predicted stress-strain curves basically coincide with each other, especially for those in the first cycle. Fig. 14b shows the stress-strain curves predicted at strain rate 1×10^{-4}/s for the polycrystalline aggregates with the [111]-type texture. It is seen that the start stress of martensite transformation in the repeated compression-unloading (about 620MPa in the 1st cycle and 340MPa in the 40th cycle) is much higher than that in the repeated tension-unloading (about 490MPa in the 1st cycle and 220MPa in the 40th cycle), and the width of the hysteresis loop in the repeated compression-unloading is larger, while the maximum transformation strain and the residual strain are smaller than that in the repeated tension-unloading. These phenomena are consistent with that observed by Kang et al. (2009). Figs. 15a and 15b show the evolution curves of temperature at the strain rate of 1×10^{-4}/s. Similar to the stress-strain curves, the evolution curves of temperature in the repeated tension-unloading coincide with that in the repeated compression-unloading. However, the oscillation of temperature in the repeated compression-unloading is stronger than that in the repeated tension-unloading.

Figs. 16a and 16b show the stress-strain curves predicted in the repeated tension-unloading and compression-unloading and at the strain rate of 5×10^{-3}/s for the un-textured and textured polycrystalline aggregates, respectively. The transformation hardening is observed in all of the cases. Figs. 17a and 17b show the evolution curves of predicted temperature under the corresponding loading conditions. It is seen that for the textured polycrystalline aggregates, the evolution curve of predicted temperature in the repeated compression-unloading is different from that in the repeated tension-unloading significantly, i.e., the oscillation of temperature is weak in the initial cycles, but becomes much stronger after certain cycles. As discussed in Section 5.1, the oscillation of temperature is mainly caused by the release/absorption of transformation latent heat during the cyclic deformation. From Fig. 16b, it is seen that in the first cycle, the martensite transformation is not completed in the compression due to the high hardening modulus. Thus, the latent heat cannot be released completely, which leads to a weak oscillation of predicted temperature. However, the start stress of martensite transformation decreases gradually during the cyclic deformation, the

martensite transformation can be completed after certain cycles. In this case, the oscillation of temperature is much stronger than that in the initial cycles.

5.3 Heterogeneity of stress-strain field in polycrystalline aggregates

It is well-known that the stress and strain fields in the polycrystalline material are inhomogeneous during the deformation. In this section, three single crystal grains with different crystallographic orientations are extracted from the polycrystalline aggregates represented by 40 random single crystal grains (which is used to model the polycrystalline NiTi shape memory alloy in Section 4.2). Thus, the material parameters used in this section are as the same as those listed in Table 1. For the chosen three grains (denoted as the grains 1, 2 and 3, respectively), their orientations of [0.1817, 0.7236, 0.6658], [$\overline{0.004}$, 0.3800, $\overline{0.9250}$] and [$\overline{0.6135}$, 0.7782, $\overline{0.1345}$] are set to be parallel to the loading direction, and then the Schmit factors of these crystallographic orientations in the tension are 0.4746, 0.3442 and 0.4534, respectively. Figs. 18a and 18b show the stress-strain curves of three prescribed grains in the 1st and 40th cycles and at the strain rate of 1×10^{-4}/s. From Fig. 18a, it is seen that the maximum stresses are about 780MPa (lower than the maximum macroscopic stress, i.e., 800MPa), 830MPa (higher than the macroscopic one) and 795MPa (close to the macroscopic one) for the grains 1, 2 and 3, respectively. Oppositely, the maximum strains are about 7.8% (larger than the maximum macro stress, i.e, 7.1%), 6.2% (smaller than the macro one) and 7.2% (close to the macro one) for the grains 1, 2 and 3, respectively. Furthermore, the start stress of martensite transformation for the grain 2 is the highest and for the grain 1 is the lowest one, which are consistent with the calculated Schmit factors of the prescribed grains. From Fig. 18b, it is seen that the residual strain of the grain 1 (about 1.6%) is much smaller than that of the grains 2 and 3 (about 2%). Figs. 19(a) and 19(b) show the evolution curves for the volume fraction of residual martensite and amount of friction slipping at the strain rate of 1×10^{-4}/s. Similarly, the saturated values for the volume fraction of residual martensite and amount of friction slipping for the grain 1 are the largest and for the grain 3 are the smallest ones. Figs. 20 and 21 show the corresponding predictions obtained by the proposed model at the strain rate of 5×10^{-3}/s. It is seen that the predicted evolution rules of the volume fraction of

residual martensite and amount of friction slipping at the strain rate of 5×10^{-3}/s are almost the same as those predicted at the strain rate of 1×10^{-4}/s. Additional transformation hardening is also predicted, similar to that observed in the polycrystalline NiTi shape memory alloy.

6. Conclusions

In this paper, a cyclic crystal plasticity based constitutive model (Yu et al., 2013) is extended to describe the rate-dependent cyclic deformation of super-elastic NiTi shape memory alloy by considering both the transformation ratchetting and internal heat production. Two sources of internal heat production are included in the proposed model, i.e., the mechanical dissipations of inelastic deformation and the transformation latent heat of the NiTi shape memory alloy. With the assumption of uniform temperature field, a simplified evolution equation of temperature field is obtained by the first law of thermodynamics and the heat boundary condition. The scale-transition rule proposed by Berveiller and Zaoui (1978) is adopted to extend the single crystal model to the polycrystalline version. It is seen that the proposed model describes the rate-dependent transformation ratchetting of super-elastic NiTi shape memory alloy reasonably. The effect of initial texture on the rate-dependent transformation ratchetting and the heterogeneity of stress and strain fields in the polycrystalline alloy are discussed. Other useful conclusions are given also by the proposed model as follows:

(1) The evolution of mean temperature is governed by both the transformation latent heat and mechanical dissipation at the intermediate frequencies, but is mainly governed by the mechanical dissipation at the high frequency. However, the oscillation of temperature is only govern by the transformation latent heat at all of the prescribed loading frequencies.

(2) The [111]-type initial texture influences the rate-dependent cyclic deformation of the NiTi shape memory alloy remarkably, i.e.: the start stress of martensite transformation in the repeated compression-unloading is much higher than that in the repeated tension-unloading, and the width of the hysteresis loop in the repeated compression-unloading is larger, but the maximum transformation strain and the residual strain are smaller than that in the repeated tension-unloading.

(3) The discrepancies between the experimental and predicted results of transformation hardening and temperature become to be more and more apparent with the increasing strain rate. It means that the proposed model should be improved by considering the temperature dependent transformation hardening and the nonlinear relation between the transformation stress and temperature after more systematic experimental data are obtained.

It should be noted that only a crystal plasticity framework is constructed in this work by considering both the transformation ratchetting and internal heat production, while many microstructure factors are not been incorporated in the proposed model, since such factors and their evolution features during the cyclic deformation of super-elastic NiTi shape memory alloy have not been clearly realized now. The micro-mechanism of the rate-dependent cyclic deformation of the NiTi alloy should be investigated in the further experimental observations, and then a real physical-mechanism model can be constructed by extending the proposed crystal plasticity framework in this work.

Acknowledgements

Financial supports by the National Natural Science Foundation of China (11025210; 11202171), the project for Sichuan Provincial Youth Science and Technology Innovation Team, China (2013TD0004), the Cultivation Foundation of Excellent Doctoral Dissertation of Southwest Jiaotong University (2013) and the Fundamental Research Funds for the Central Universities, China, are appreciated.

References

Anand, L., Gurtin, M.E., 2003. Thermal effects in the superelasticity of crystalline shape-memory materials. J. Mech. Phys. Solids 51, 1015-1058.

Auricchio, F., Marfia, S., Sacco, E., 2003. Modelling of SMA materials: training and two way memory effects. Comp. Struct. 81, 2301-2317.

Auricchio, F., Reali, A., Stefanelli, U., 2007. A three-dimensional model describing stress-induced solid phase transformation with permanent inelasticity. Int. J. Plasticity 23, 207-226.

Berveiller, M., Zaoui, A., 1978. An extension of the self-consistent scheme to plastically-flowing polycrystals. J. Mech. Phys. Solids 26, 325-344.

Bo, Z., Lagoudas, D.C., 1999a. Thermomechanical modelling of polycrystalline SMAs under cyclic loading, Part I: theoretical derivations. Int. J. Eng. Sci. 37, 1089-1140.

Bo, Z., Lagoudas, D.C., 1999b. Thermomechanical modelling of polycrystalline SMAs under cyclic loading, Part III: evolution of plastic strains and two-way memory effect. Int. J. Eng. Sci. 37, 1141-1173.

Bo, Z., Lagoudas, D.C., 1999c. Thermomechanical modelling of polycrystalline SMAs under cyclic loading, Part IV: modelling of minor hysteresis loops. Int. J. Eng. Sci. 37, 1174-1204.

Brinson, L. C., Schmidt, I., Lammering, R., 2004. Stress-induced transformation behavior of a polycrystalline NiTi shape memory alloy: micro and macromechanical investigations via in situ optical microscopy. J. Mech. Phys. Solids 52, 1549-1571.

Christ, D., & Reese, S., 2009. A finite element model for shape memory alloys considering thermomechanical couplings at large strains. Int. J. Solids. Struct. 46, 3694-3709.

Gall, K., Sehitoglu, H., 1999. The role of texture in tension–compression asymmetry in polycrystalline NiTi. Int. J. Plasticity 15, 69-92.

Gall, K., Lim, T.J., McDowell, D.L., Sehitoglu, H., Chumlyakov, Y., 2000. The role of intergranular constraint on the stress-induced martensitic transformation in textured polycrystalline NiTi. Int. J. Plasticity 16, 1189-1214.

Gall, K., Maier, H.J., 2002. Cyclic deformation mechanisms in precipitated NiTi shape memory alloys. Acta. Mater. 50, 4643-4657.

Gao, X.J., Huang, M., Brinson, L., 2000. A multivariant micromechanical model for SMAs Part 1. Crystallographic issues for single crystal model. Int. J. Plasticity 16, 1345-1369.

Grabe, C., O. T. Bruhns., 2008. On the viscous and strain rate dependent behavior of polycrystalline NiTi. Int. J. Solids. Struct. 45, 1876-1895.

Guthikonda V.S., Elliott R.S., 2013. Modeling martensite transformations in shape memory alloys with the self-consistent lattice dynamics approach. J. Mech. Phys. Solids 61, 1010-1026.

He, Y.J., Sun, Q.P., 2010a. Rate-dependence domain spacing in a stretched NiTi strip. Int. J. Solids Struct. 47, 2775-2783.

He, Y.J., Sun, Q.P., 2010b. Frequency-dependent temperature evolution in NiTi shape memory alloy under cyclic loading. Smart Mater. Struct. 19, 115014.

He, Y.J., Yin, H., Zhou, R.H., Sun, Q.P., 2010c. Ambient effect on damping peak of NiTi shape memory alloy. Mater. Lett. 64, 1483-1486.

He, Y.J., Sun, Q.P., 2011. On non-monotonic rate dependence of stress hysteresis of superelastic shape memory alloy bars. Int. J. Solids Struct. 48, 1688-1695.

Huang, M., Brinson, L.C., 1998. A multivariant model for single crystal shape memory alloy behavior. J. Mech. Phys. Solids 46, 1379-1409.

Huang, M., Gao, X.J., Brinson, L.C., 2000. A multivariant micromechanical model for SMAs Part 2. Polycrystal model. Int. J. Plasticity 16, 1371-1390.

Kan, Q.H., Kang, G.Z., 2010. Constitutive model for uniaxial transformation ratchetting of super-elastic NiTi shape memory alloy at room temperature. Int. J. Plasticity 26, 441-465.

Kang, G.Z., Kan, Q.H., Qian, L.M., Liu, Y.J., 2009. Ratchetting deformation of superelastic and shape memory NiTi Alloys. Mech. Mater. 41, 139-153.

Kang, G.Z., Bruhns, O.T. , Sai, K., 2011. Cyclic polycrystalline visco-plastic model for ratchetting of 316L stainless steel. Comput. Mater. Sci. 50, 1399-1405.

Kang, G.Z., Kan, Q.H., Yu, C., Song, D., Liu, Y.J., 2012. Whole-life transformation ratchetting and fatigue of super-elastic NiTi Alloy under uniaxial stress-controlled cyclic loading. Mater. Sci. Eng. A 535, 228-234.

Kröner, E., 1961. Zur plastischen verformung des vielkristalls. Acta Metall. 9, 155–161.

Lagoudas, D.C., Bo, Z., 1999. Thermomechanical modelling of polycrystalline SMAs under cyclic loading, Part II: material characterization and experimental results for a stable transformation cycle. Int. J. Eng. Sci. 37, 1205-1249.

Lagoudas, D.C., Entchev, P.B., 2004. Modelling of transformation-induced plasticity and its effect on the behaviour of porous shape memory alloys. Part I: constitutive model for fully dense SMAs. Mech. Mater. 36, 865-892.

Lagoudas, D.C., Entchev, P.B., Popov, P., Patoor, E., Brinson, L.C., Gao, X.J., 2006. Shape memory alloys, Part II: modelling of polycrystals. Mech. Mater. 38, 430-462.

Levitas, V.I., Ozsoy, I.B., 2009a. Micromechanical modeling of stress-induced phase transformations. Part 1. Thermodynamics and kinetics of coupled interface propagation and reorientation. Int. J. Plasticity 25, 239-280.

Levitas, V.I., Ozsoy, I.B., 2009b. Micromechanical modeling of stress-induced phase transformations. Part 2. Computational algorithms and examples. Int. J. Plasticity 25, 546-583.

Levitas, V.I., 2013. Thermodynamically consistent phase field approach to phase transformations with interface stresses. Acta Mater. 61, 4305-4319.

Lexcellent, C., Leclerq, S., Gabry, B., Bourbon, G., 2000. The two way shape memory effect of shape memory alloys: an experimental study and a phenomenological model. Int. J. Plasticity 16, 1155-1168.

Morgan, N.B., 2004. Medical shape memory alloy applications - the market and its products. Mater. Sci. Eng. A 378, 16-23.

Manchiraju, S., Anderson, P.M., 2010. Coupling between martensitic phase transformations and plasticity: A microstructure-based finite element model. Int. J. Plasticity 26, 1508–1526.

Morin, C., Moumni, Z., Zaki, W., 2011a. A constitutive model for shape memory alloys accounting for thermomechanical coupling. Int. J. Plasticity 27, 748-767.

Morin, C., Moumni, Z., Zaki, W., 2011b. Thermomechanical coupling in shape memory alloys under cyclic loadings: Experimental analysis and constitutive modeling. Int. J. Plasticity 27, 1959-1980.

Nae, F.A., Matsuzaki, Y., Ikeda, T., 2003. Micromechanical modeling of polycrystalline shape-memory alloys including thermo-mechanical coupling. Smart Mater. Struct. 12, 6-17.

Nemat-Nasser, S., Guo, W.G., 2006. Superelastic and cyclic response of NiTi SMA at various strain rates and temperatures. Mech. Mater. 38, 463-474.

Otsuka, K., Ren, X., 2005. Physical metallurgy of Ti–Ni-based shape memory alloys. Progr.

Mater. Sci. 50, 511-678.

Patoor, E., Eberhardt, A., Berveiller, M., 1996. Micromechanical modelling of superelasticity in shape memory alloys. J. Phys. IV 6. C1-277–C1-292.

Patoor, E., Lagoudas, D.C., Entchev, P.B., Brinson, L.X., Gao, X., 2006. Shape memory alloys, Part I: General properties and modeling of single crystals. Mech. Mater. 38, 391-429.

Peigney, M., Seguin, J. P., 2013. An incremental variational approach to coupled thermo-mechanical problems in anelastic solids. Application to shape-memory alloys. Int. J. Solids Struct. 50, 4043-4054.

Sehitoglu, H., Anderson, R., Karaman, L., Gall, K., Chumlyakov, Y., 2001. Cyclic deformation behaviour of single crystal NiTi. Mater. Sci. Eng. A 314, 67-74.

Shaw, J.A., Kyriakides, S., 1995. Thermomechanical aspects of NiTi. J. Mech. Phys. Solids 43,1243-1281.

Sun, Q.P., Hwang, K.C., 1993a. Micromechanics modelling for the constitutive behaviour of polycrystalline shape memory alloys-I. Derivation of general relations. J. Mech. Phys. Solids 41, 1-17.

Sun, Q.P., Hwang, K.C., 1993b. Micromechanics modelling for the constitutive behaviour of polycrystalline shape memory alloys-II: study of the individual phenomena. J. Mech. Phys. Solids 41, 19-33.

Sun, Q.P., Li, Z.Q., 2002. Phase transformation in superelastic NiTi polycrystalline micro-tubes under tension and torsion-from localization to homogeneous deformation. Int. J. Solids. Struct. 39, 2797-3809.

Sun, Q.P., Zhao, H., Zhou, R., Saletti, D., Yin, H., 2012. Recent advances in spatiotemporal evolution of thermomechanical fields during the solid-solid phase transition. Compt. Rend. Mecanique 340, 349-358.

Thamburaja, P., Anand, L., 2001. Polycrystalline shape-memory alloys: Effect of crystallographic texture. J. Mech. Phys. Solids 49, 709-737.

Thamburaja, P., Anand, L., 2003. Thermo-mechanically coupled superelastic response of initially-textured Ti-Ni sheet. Acta. Mater. 51, 325-338.

Thamburaja, P., Pan, H., Chau, F.S., 2005. Martensitic reorientation and shape-memory effect in initially-textured polycrystalline Ti-Ni sheet. Acta. Mater, 53, 3821-3831.

Thamburaja, P., Pan, H., Chau, F.S., 2009. The evolution of microstructure during twinning: Constitutive equations, finite-element simulations and experimental verification. Int. J. Plasticity 25, 2141-2168.

Vitiello, A., Giorleo, G., Morace, R.E., 2005. Analysis of thermomechanical behaviour of Nitinol wires with high strain rates. Smart Mater. Struct. 14, 215.

Wang, X.M., Xu, B.X., Yue, Z.F., 2008. Micromechanical modelling of the effect of plastic deformation on the mechanical behaviour in pseudoelastic shape memory alloys. Int. J. Plasticity, 24, 1307-1332.

Yin, H., Sun, Q.P., 2012. Temperature variation in NiTi shape memory alloy during cyclic phase transition. J. Mater. Eng. Perform. DOI : 10.1007/s11665-012-0395-9.

Yin, H., Yan, Y., Huo, Y.Z, Sun, Q.P. 2013. Rate dependent damping of single crystal CuAlNi shape memory alloy. Mater. Lett. 109, 287-290.

Yin, H., He, Y.J., Sun, Q.P., 2014. Effect of deformation frequency on temperature and stress oscillations in cyclic phase transition of NiTi shape memory alloy. J. Mech. Phys. Solids, http://dx.doi.org/10.1016/j.jmps.2014.01.013.

Yu, C., Kang, G.Z., Song, D., Kan, Q.H., 2012. Micromechanical constitutive model considering plasticity for super-elastic NiTi shape memory alloy. Comput. Mater. Sci. 56, 1-5.

Yu, C., Kang, G.Z., Kan, Q.H., Song, D., 2013. A micromechanical constitutive model based on crystal plasticity for thermo-mechanical cyclic deformation of NiTi shape memory alloys. Int. J. Plasticity 44, 161-191.

Yu, C., Kang, G.Z., Kan, Q.H., 2014. Crystal plasticity based constitutive model of NiTi shape memory alloy considering different mechanisms of inelastic deformation. Int. J. Plasticity 54, 132-162.

Zaki, W., Moumni, Z., 2007a. A 3-D model of the cyclic thermomechanical behaviour of shape memory alloys. J. Mech. Phys. Solids 55, 2427-2454.

Zaki, W., Moumni, Z., 2007b. A three-dimensional model of the thermomechanical behavior

of shape memory alloys. J. Mech. Phys. Solids 55, 2455-2490.

Zhang, X.H., Feng. P., He, Y.J., Y, T.X., Sun, Q.P., 2010. Experimental study on rate dependence of macroscopic domain and stress hysteresis in NiTi shape memory alloy strips. Int. J. Mech. Sci. 52, 1660-1670.

Zhu, S.Y, Zhang Y.F., 2007. A thermomechanical constitutive model for superelastic SMA wire with strain-rate dependence. Smart. Mater. Struct. 16, 1696-1707.

Table 1 Material parameters for the NiTi shape memory alloy used by Morin et al. (2011b)

$E_A = 70\text{GPa}$; $E_M = 33\text{GPa}$; $\nu = 0.3$; $T_{ref} = 242\text{K}$; $g^{tr} = 0.11$;
$\beta = 0.35\text{MPa}$; $B_{sat} = 120\text{MPa}$; $Y_0 = 9\text{MPa}$; $Y_{sat} = 4\text{MPa}$;
$H_0 = 0\text{MPa}$; $H_{sat} = 25\text{MPa}$; $\gamma_{sat} = 0.008$; $\xi_{sat} = 0.05$; $b_1 = 3$; $b_2 = 10$;
$D = 3\text{GPa}$; $c = 29\text{MPaK}^{-1}$; $h = 110\text{Wm}^{-2}\text{K}^{-1}$;

Table 2 Material parameters for the NiTi shape memory alloy used by Sun et al. (2012)

$E_A = 28\text{GPa}$; $E_M = 20\text{GPa}$; $\nu = 0.3$;
$T_{ref} = 258\text{K}$; $g^{tr} = 0.1$; $\beta = 0.25\text{MPa}$; $Y_0 = 3.1\text{MPa}$; $H_0 = 5\text{MPa}$;
$D = 3\text{GPa}$; $c = 32.25\text{MPaK}^{-1}$; $h = 100\text{Wm}^{-2}\text{K}^{-1}$;

Figure lists

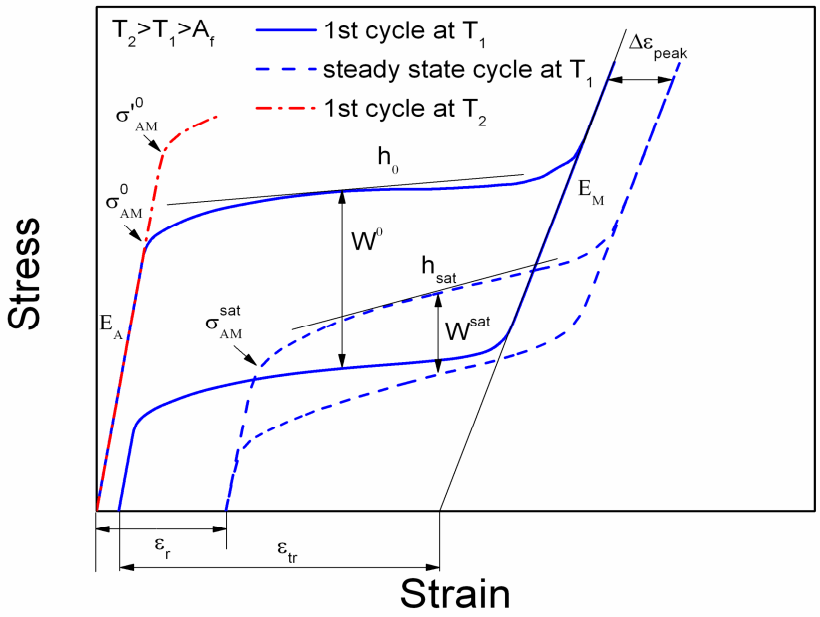

Fig. 1 Illustration for the determination of material parameters

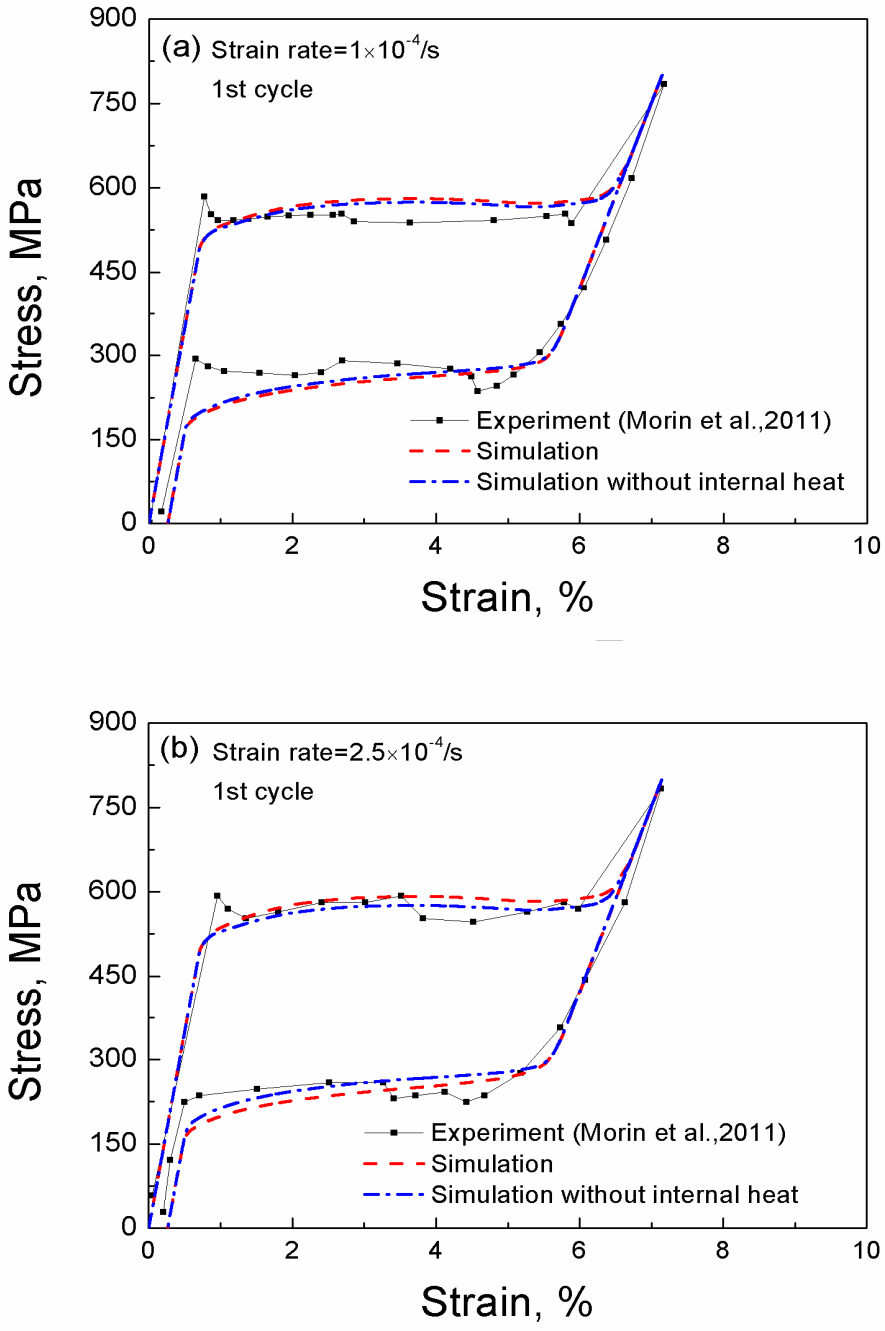

Fig. 2 Experimental and simulated stress-strain curves in the 1st cycle and at different strain rates: (a) 1×10^{-4}/s; (b) 2.5×10^{-4}/s; (c) 5×10^{-4}/s; (d) 1×10^{-3}/s; (e) 2.5×10^{-3}/s; (f) 5×10^{-3}/s.

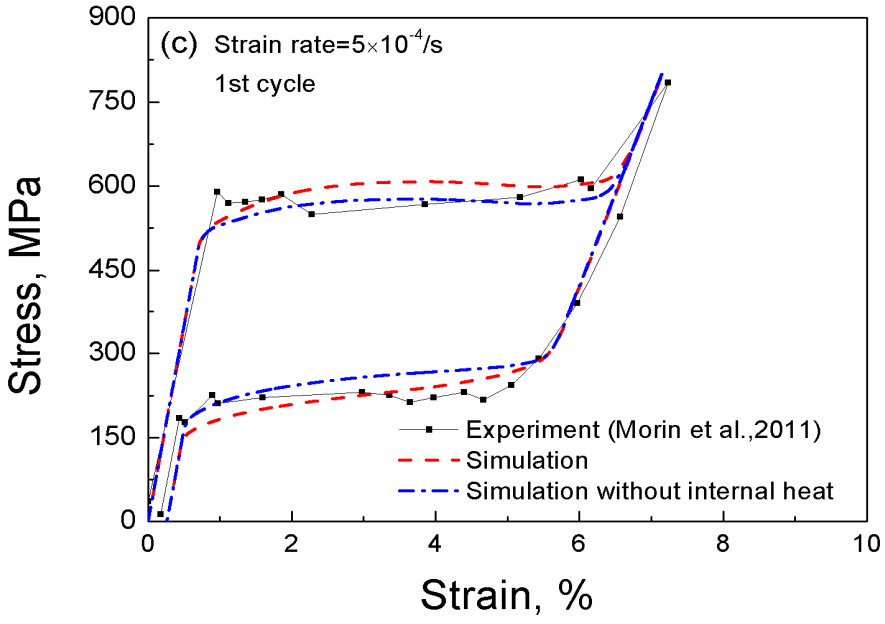

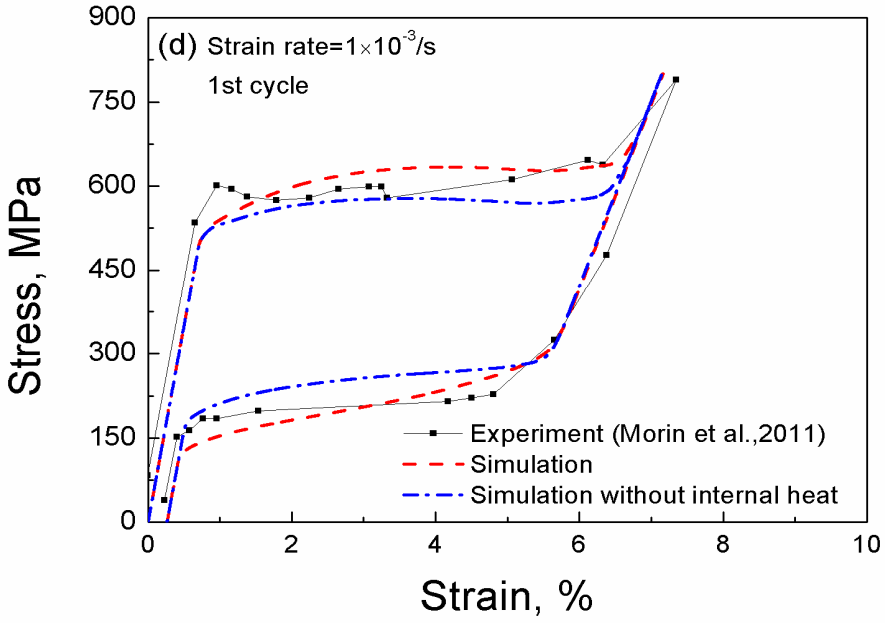

Fig. 2 (continued) Experimental and simulated stress-strain curves in the 1st cycle and at different strain rates: (a) 1×10^{-4}/s; (b) 2.5×10^{-4}/s; (c) 5×10^{-4}/s; (d) 1×10^{-3}/s; (e) 2.5×10^{-3}/s; (f) 5×10^{-3}/s.

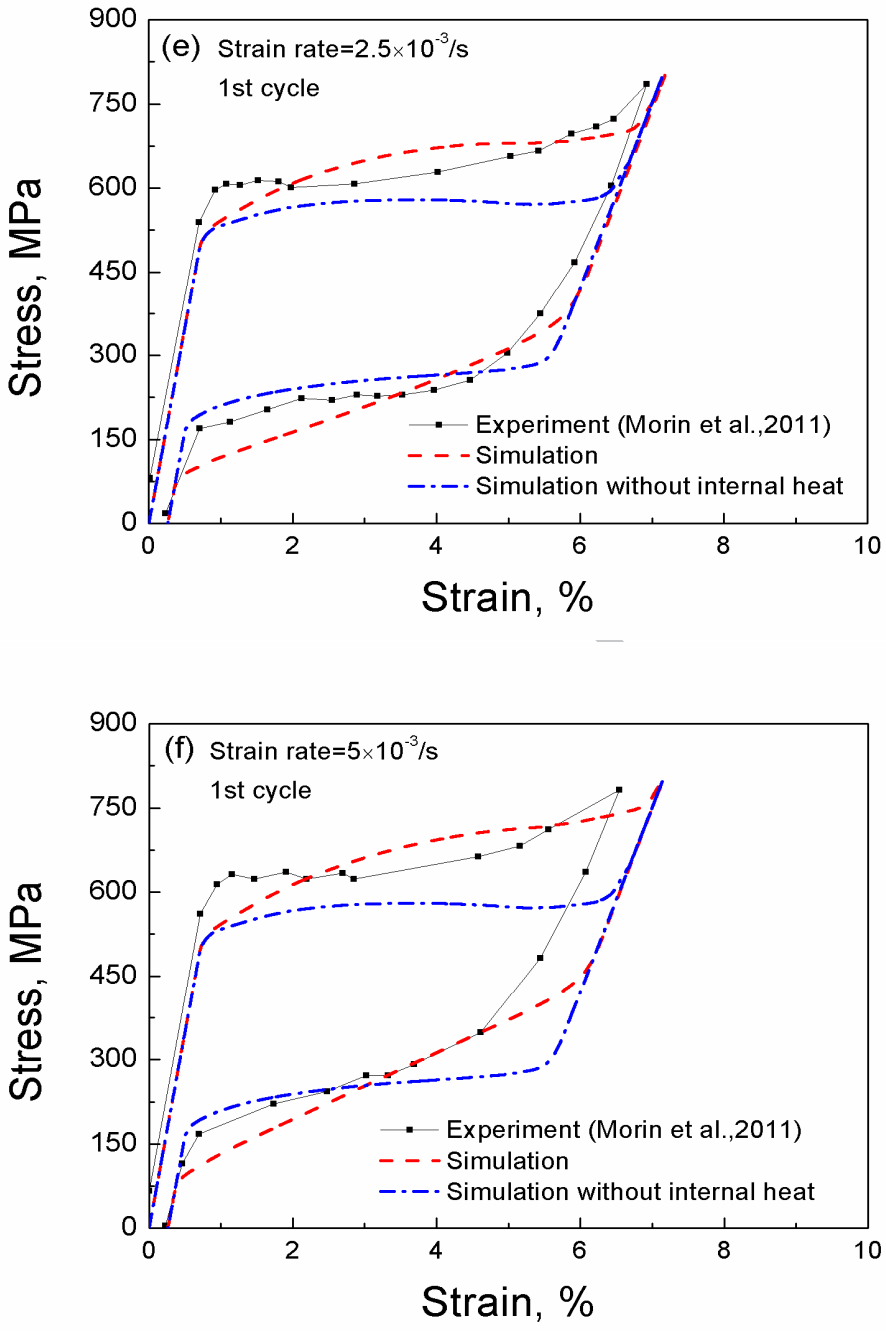

Fig. 2 (continued) Experimental and simulated stress-strain curves in the 1st cycle and at different strain rates: (a) 1×10^{-4}/s; (b) 2.5×10^{-4}/s; (c) 5×10^{-4}/s; (d) 1×10^{-3}/s; (e) 2.5×10^{-3}/s; (f) 5×10^{-3}/s.

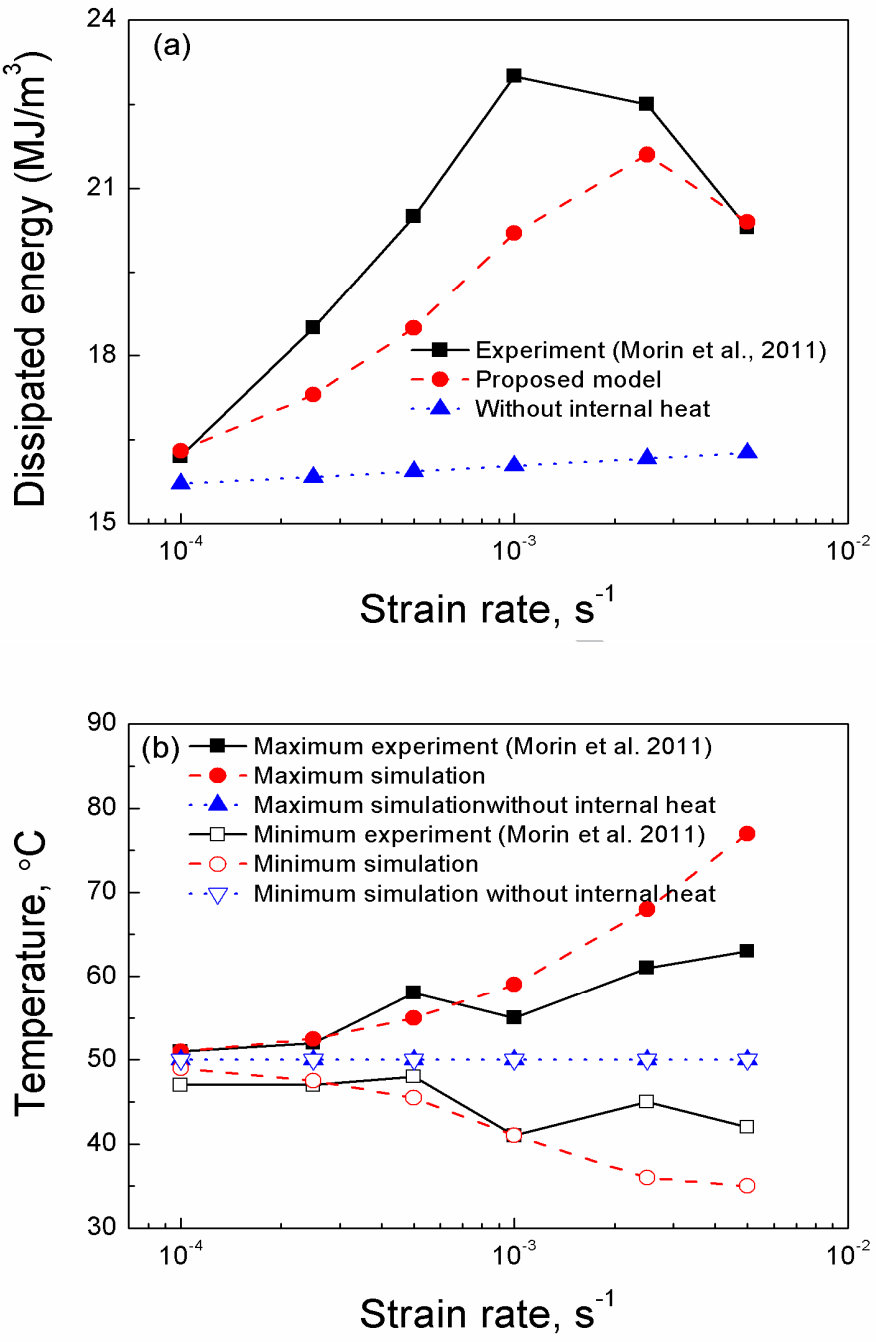

Fig. 3 Experimental and simulated results of dissipated energy and uniform temperature in the 1st cycle and at different strain rates: (a) dissipated energy vs. strain rate; (b) maximum and minimum uniform temperatures vs. strain rate.

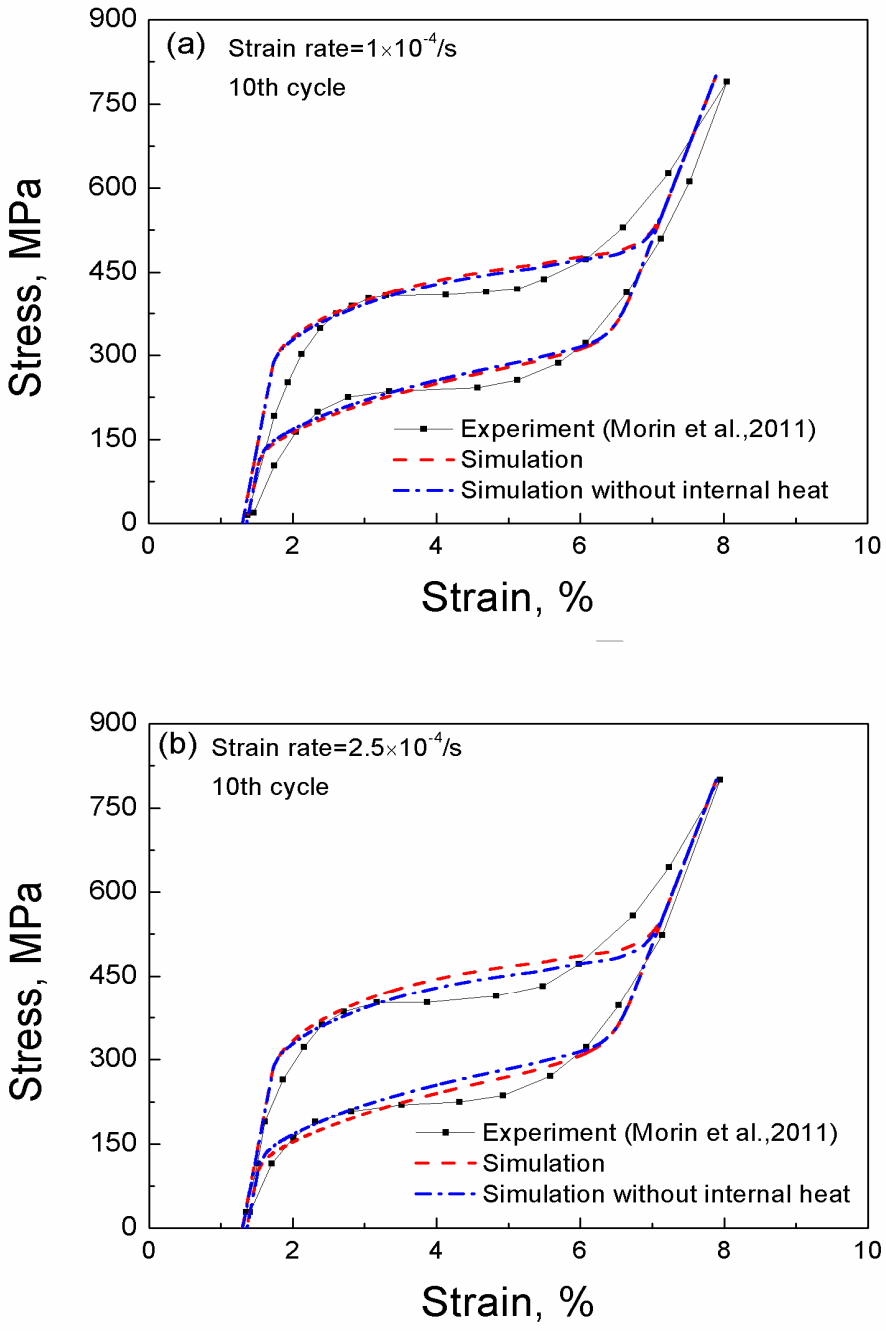

Fig. 4 Experimental and simulated stress-strain curves in the 10th cycle and at different strain rates: (a) 1×10^{-4}/s; (b) 2.5×10^{-4}/s; (c) 5×10^{-4}/s; (d) 1×10^{-3}/s; (e) 2.5×10^{-3}/s; (f) 5×10^{-3}/s.

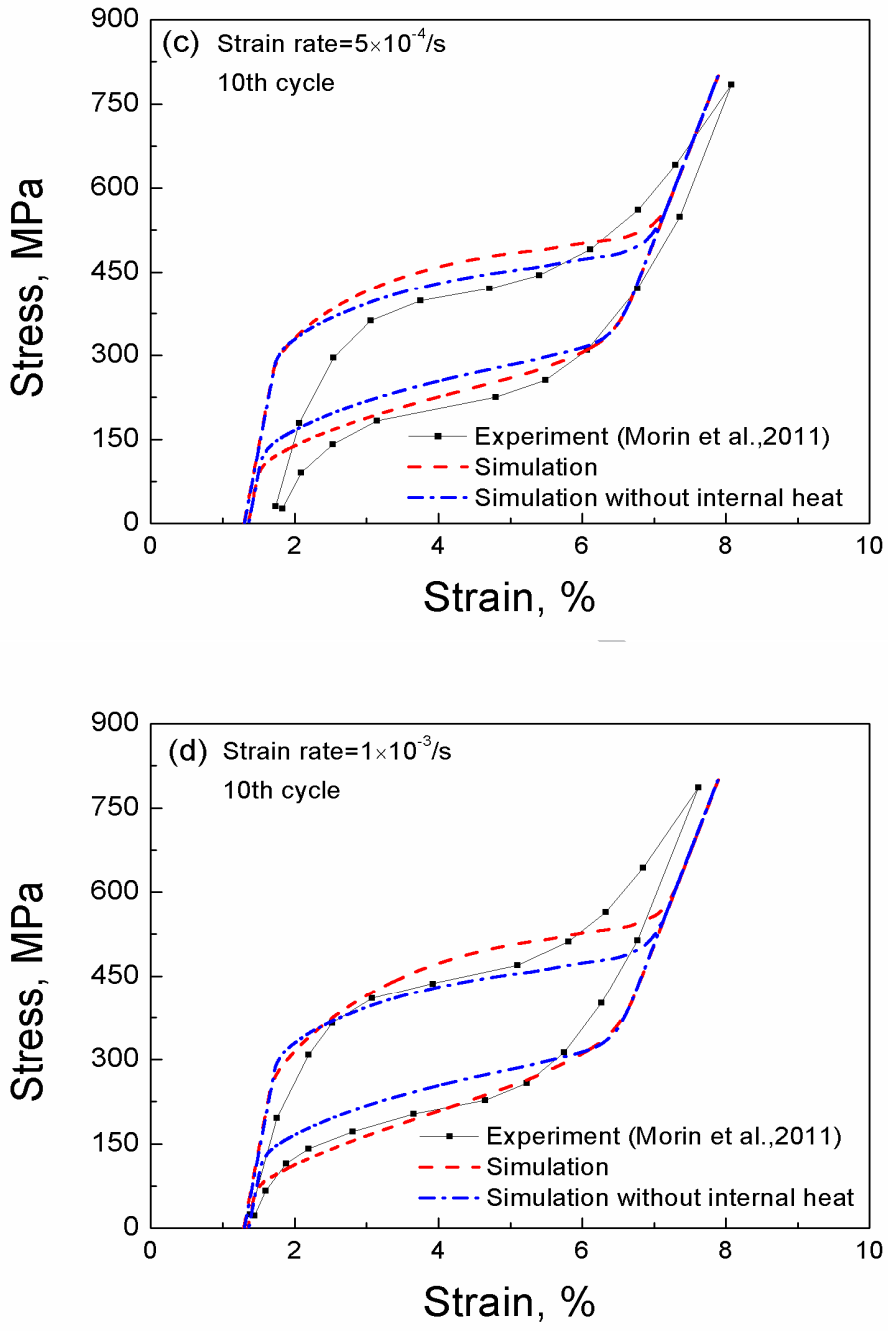

Fig. 4 (continued) Experimental and simulated stress-strain curves in the 10th cycle and at different strain rates: (a) 1×10^{-4}/s; (b) 2.5×10^{-4}/s; (c) 5×10^{-4}/s; (d) 1×10^{-3}/s; (e) 2.5×10^{-3}/s; (f) 5×10^{-3}/s.

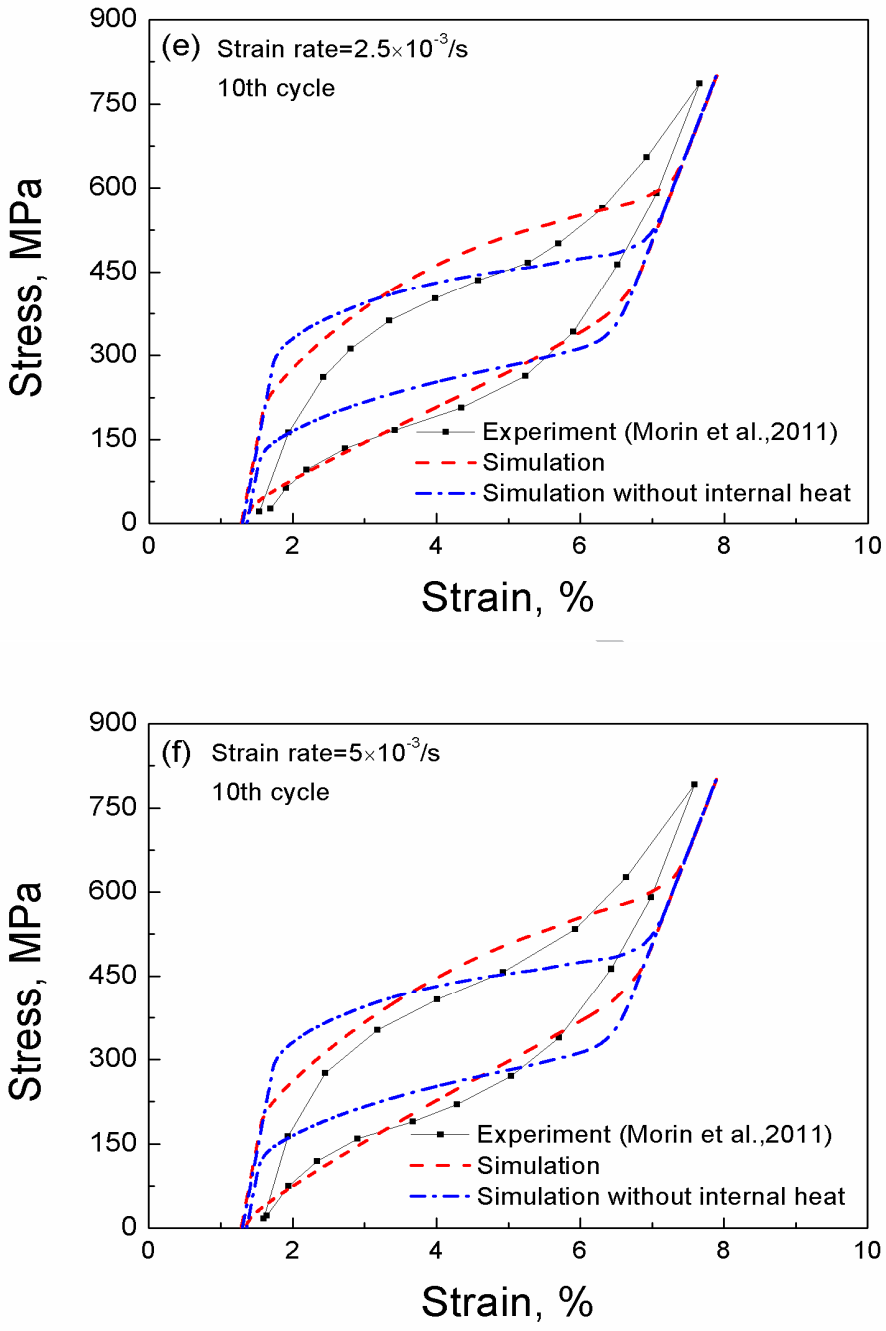

Fig. 4 (continued) Experimental and simulated stress-strain curves in the 10th cycle and at different strain rates: (a) 1×10^{-4}/s; (b) 2.5×10^{-4}/s; (c) 5×10^{-4}/s; (d) 1×10^{-3}/s; (e) 2.5×10^{-3}/s; (f) 5×10^{-3}/s.

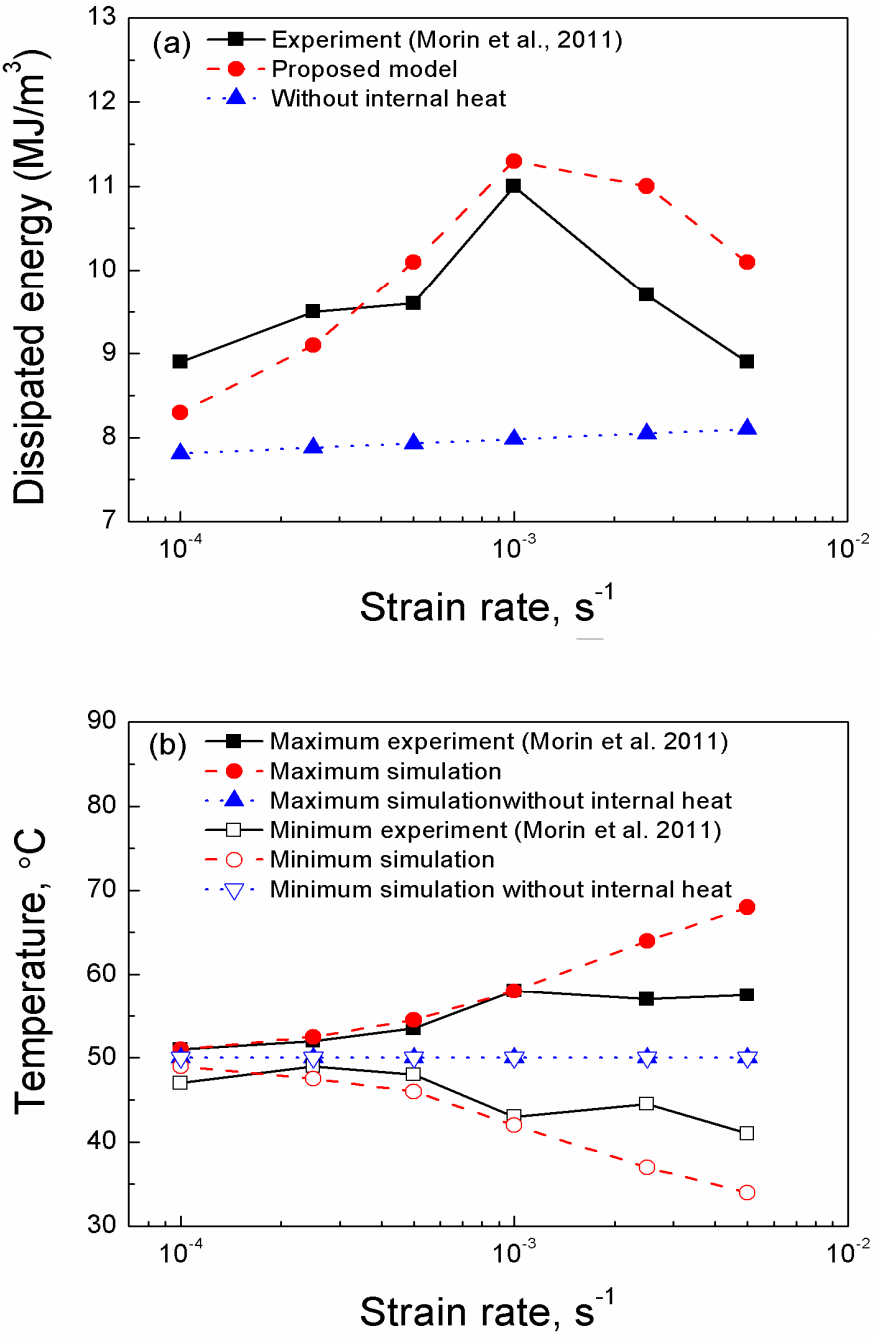

Fig. 5 Experimental and simulated results of dissipated energy and uniform temperature in the 10th cycle and at different strain rates: (a) dissipated energy vs. strain rate; (b) maximum and minimum uniform temperatures vs. strain rate.

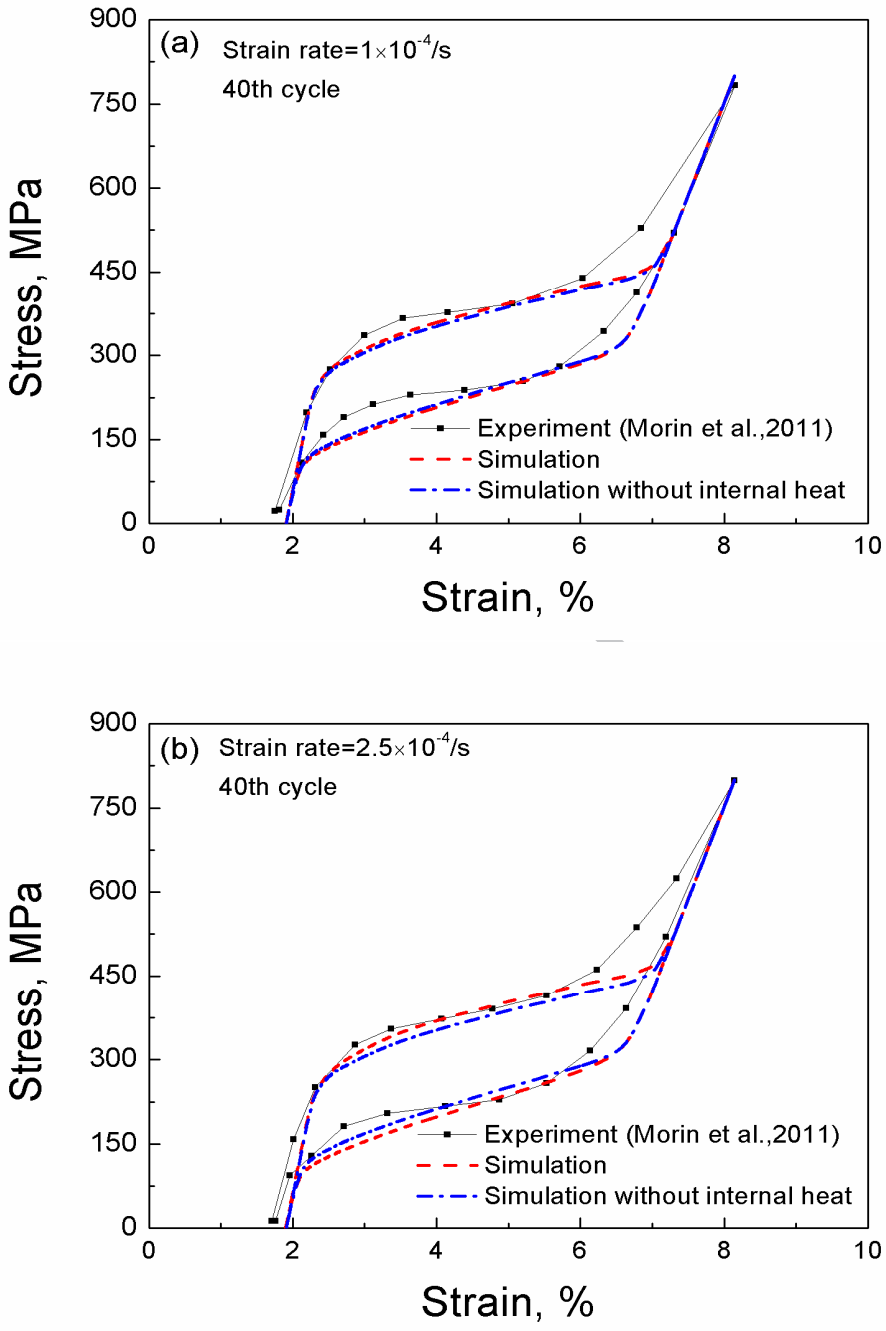

Fig. 6 Experimental and simulated stress-strain curves in the 40th cycle and at different strain rates: (a) 1×10^{-4}/s; (b) 2.5×10^{-4}/s; (c) 5×10^{-4}/s; (d) 1×10^{-3}/s; (e) 2.5×10^{-3}/s; (f) 5×10^{-3}/s.

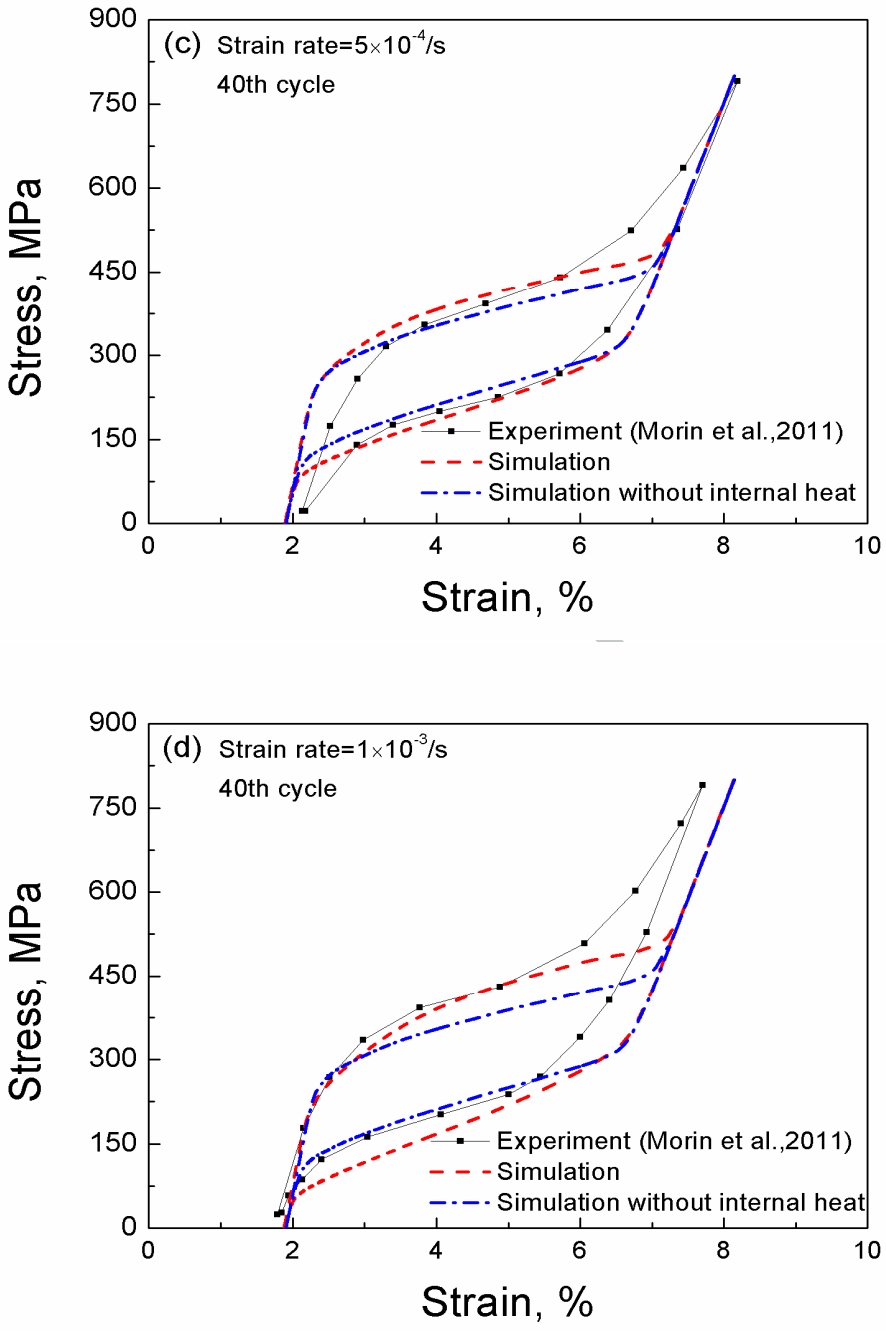

Fig. 6 (continued) Experimental and simulated stress-strain curves in the 40th cycle and at different strain rates: (a) 1×10^{-4}/s; (b) 2.5×10^{-4}/s; (c) 5×10^{-4}/s; (d) 1×10^{-3}/s; (e) 2.5×10^{-3}/s; (f) 5×10^{-3}/s.

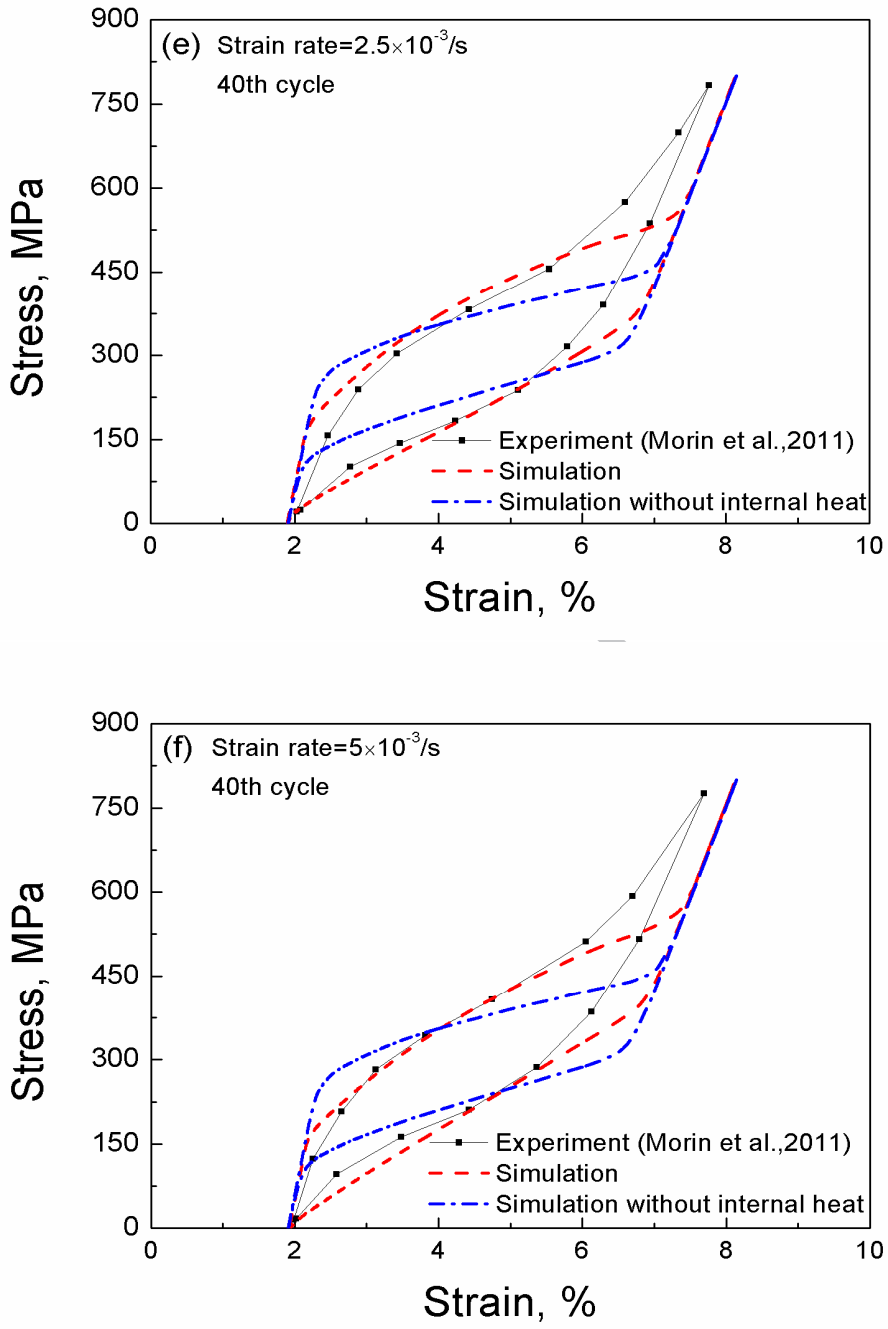

Fig. 6 (continued) Experimental and simulated stress-strain curves in the 40th cycle and at different strain rates: (a) 1×10^{-4}/s; (b) 2.5×10^{-4}/s; (c) 5×10^{-4}/s; (d) 1×10^{-3}/s; (e) 2.5×10^{-3}/s; (f) 5×10^{-3}/s.

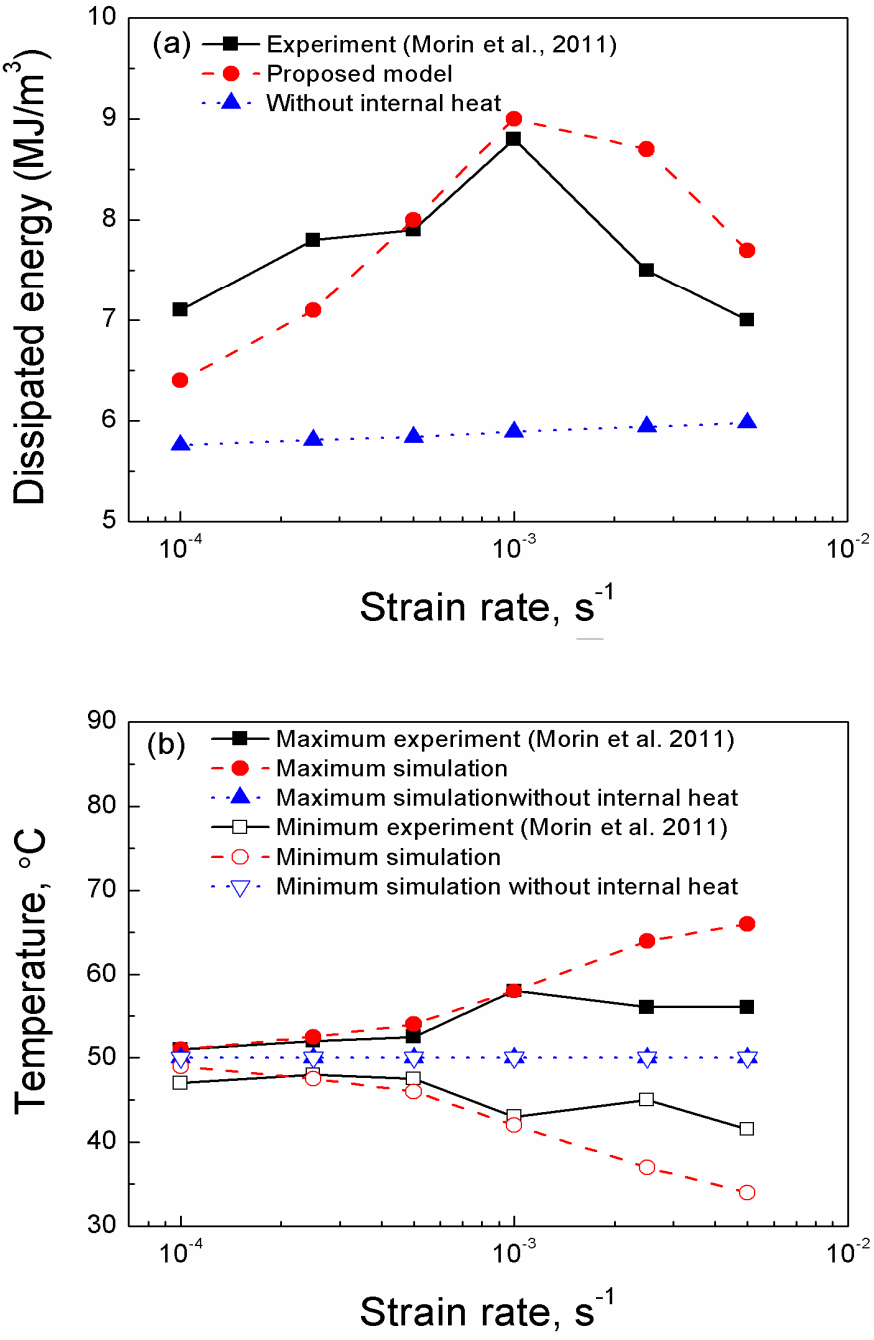

Fig. 7 Experimental and simulated results of dissipated energy and uniform temperature in the 40th cycle and at different strain rates: (a) dissipated energy vs. strain rate; (b) maximum and minimum uniform temperatures vs. strain rate.

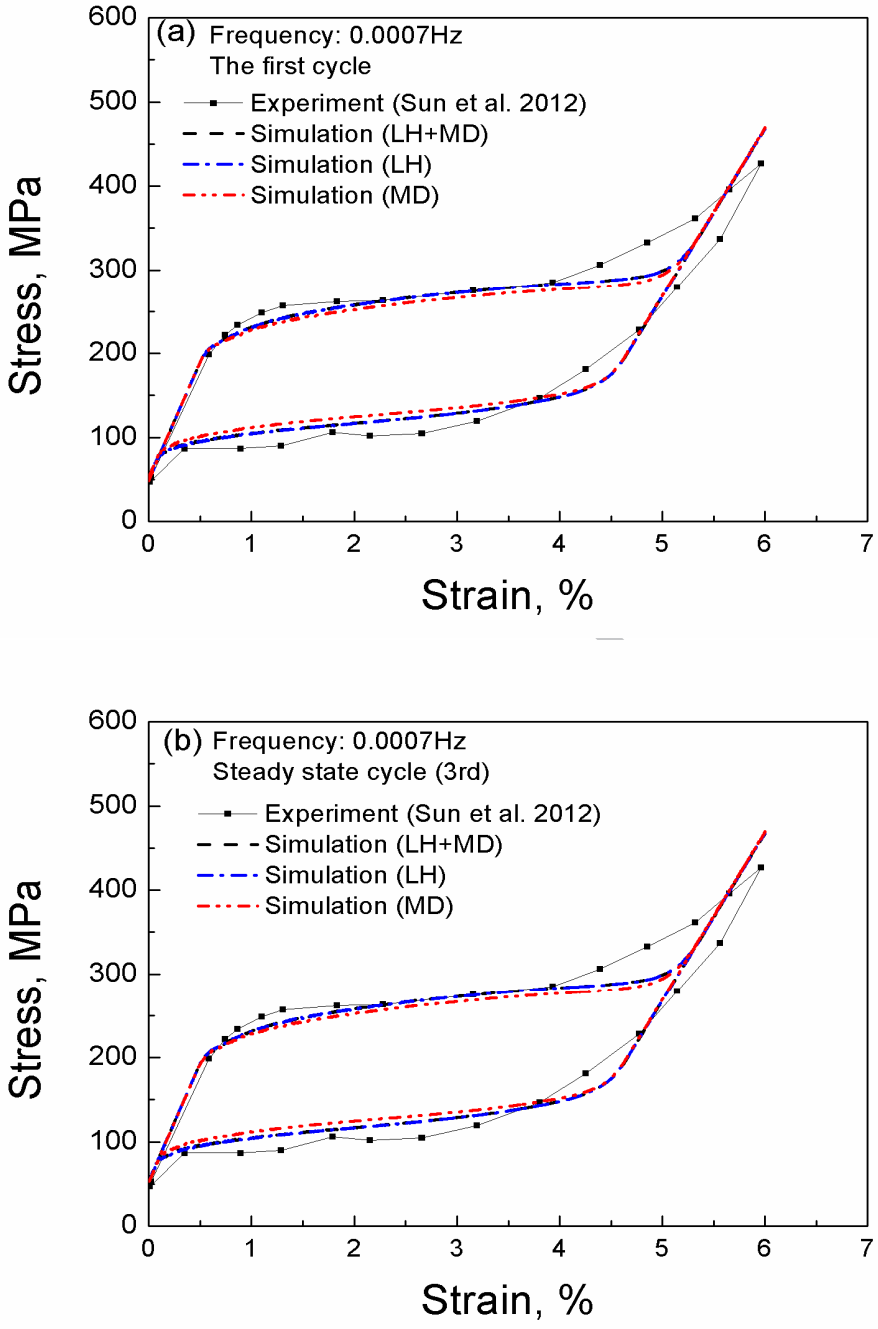

Fig. 8 Stress-strain curves at the loading frequency of 0.0007Hz: (a) in the first cycle; (b) in the steady cycle (the 3rd cycle).

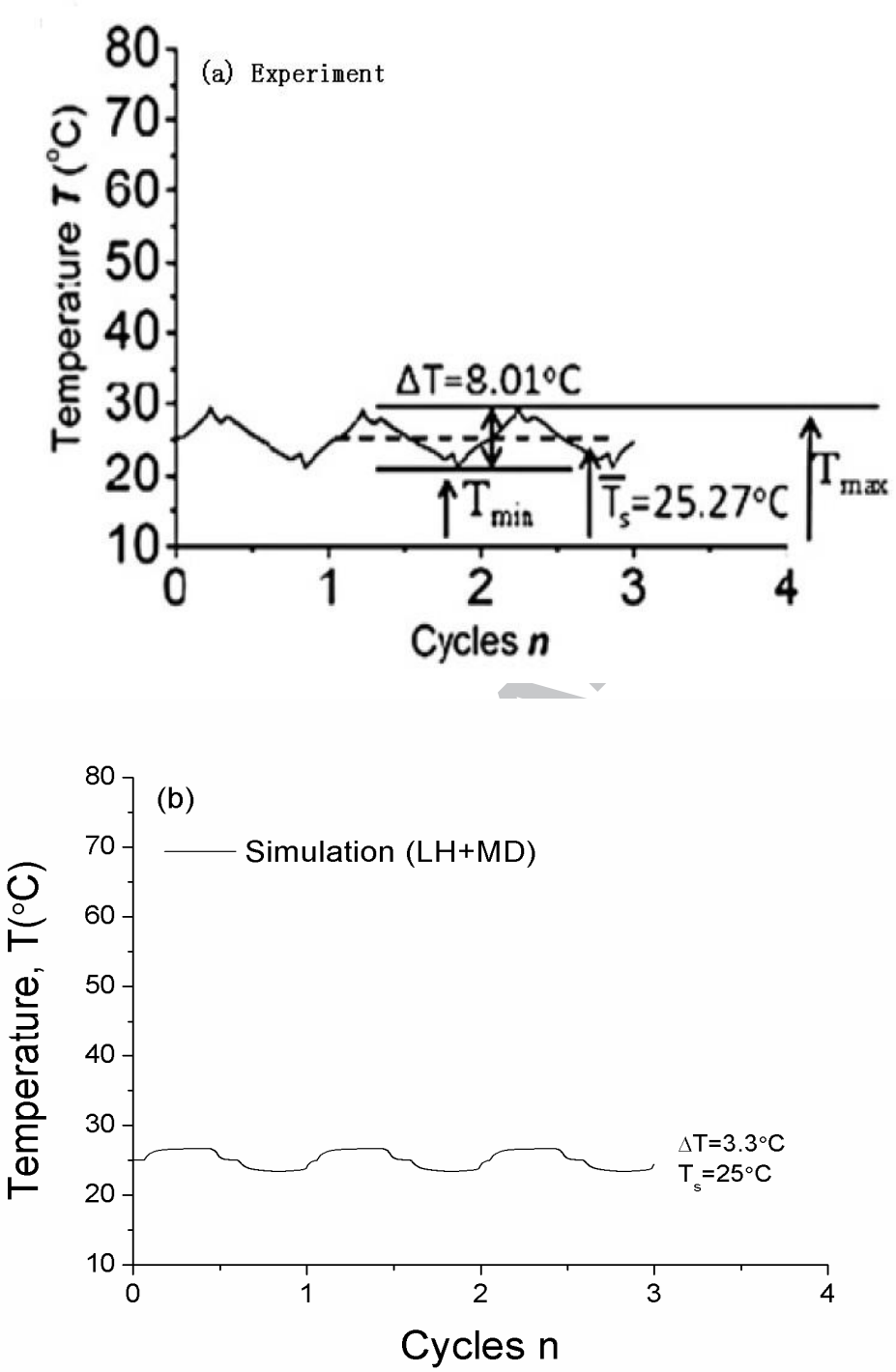

Fig. 9 Curves of temperature vs. cycles at the loading frequency of 0.0007Hz: (a) experiment (from Sun et al., 2012); (b) simulation (LH+MD); (c) simulations (LH and MD separately).

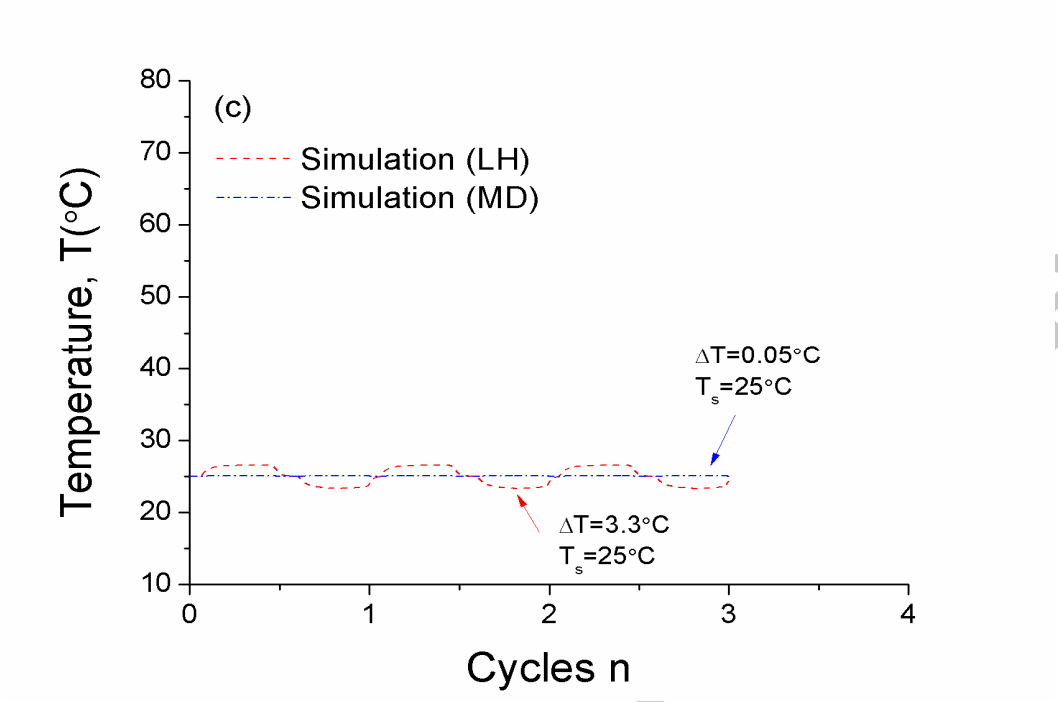

Fig. 9 (continued) Curves of temperature vs. cycles at the loading frequency of 0.0007Hz: (a) experiment (from Sun et al., 2012); (b) simulation (LH+MD); (c) simulations (LH and MD separately).

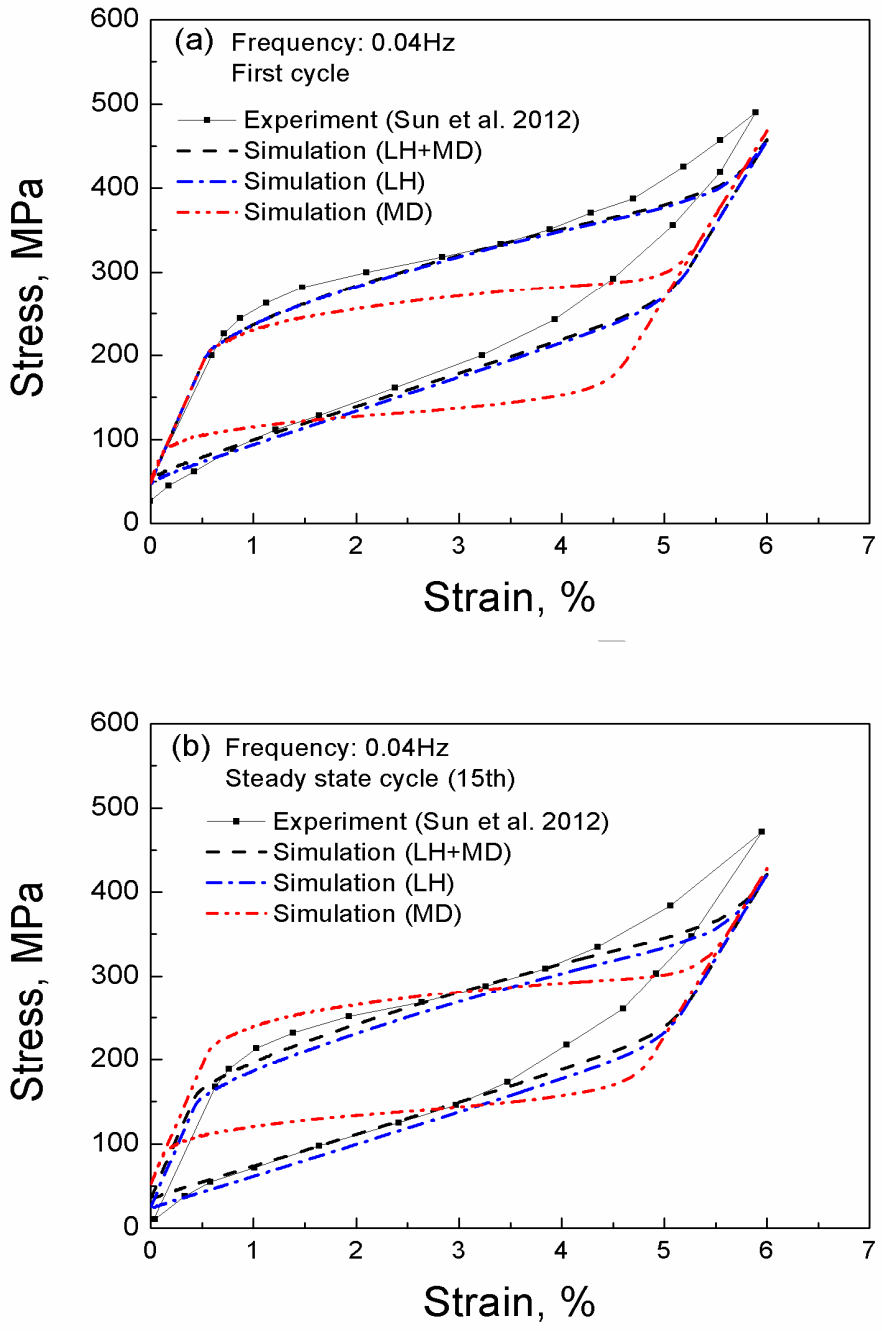

Fig. 10 Stress-strain curves at the loading frequency of 0.04Hz: (a) in the first cycle; (b) in the steady cycle (the 15th cycle).

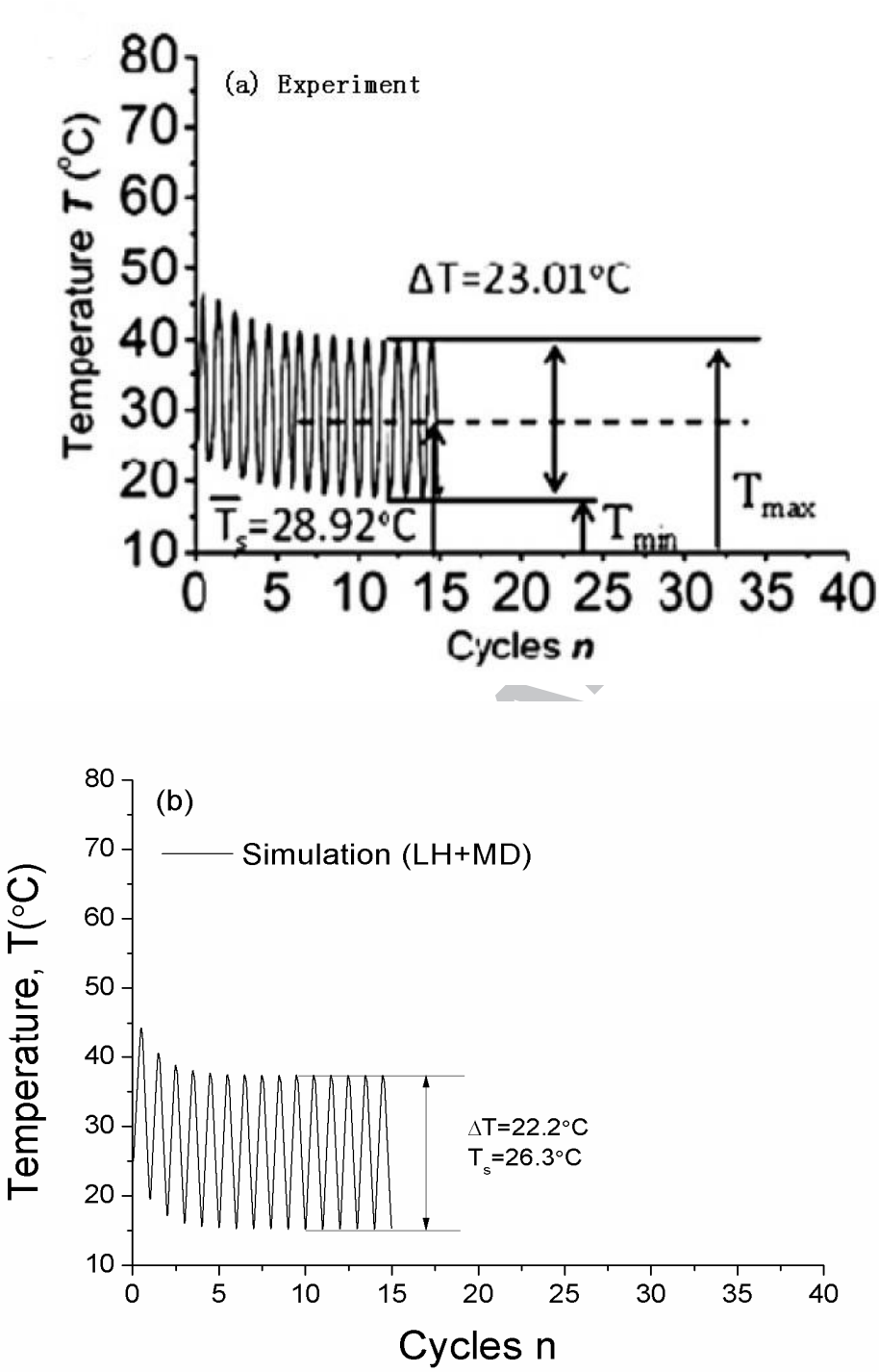

Fig. 11 Curves of temperature vs. cycles at the loading frequency of 0.04Hz: (a) experiment (from Sun et al., 2012); (b) simulation (LH+MD); (c) simulations (LH and MD separately).

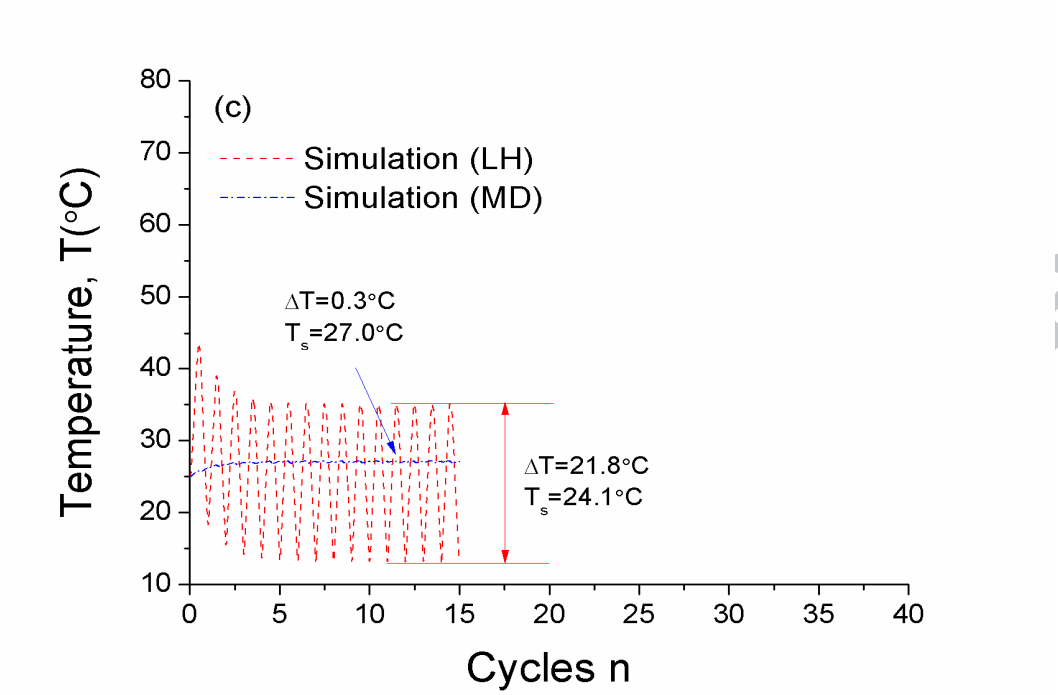

Fig. 11 (continued) Curves of temperature vs. cycles at the loading frequency of 0.04Hz: (a) experiment (from Sun et al., 2012); (b) simulation (LH+MD); (c) simulations (LH and MD separately).

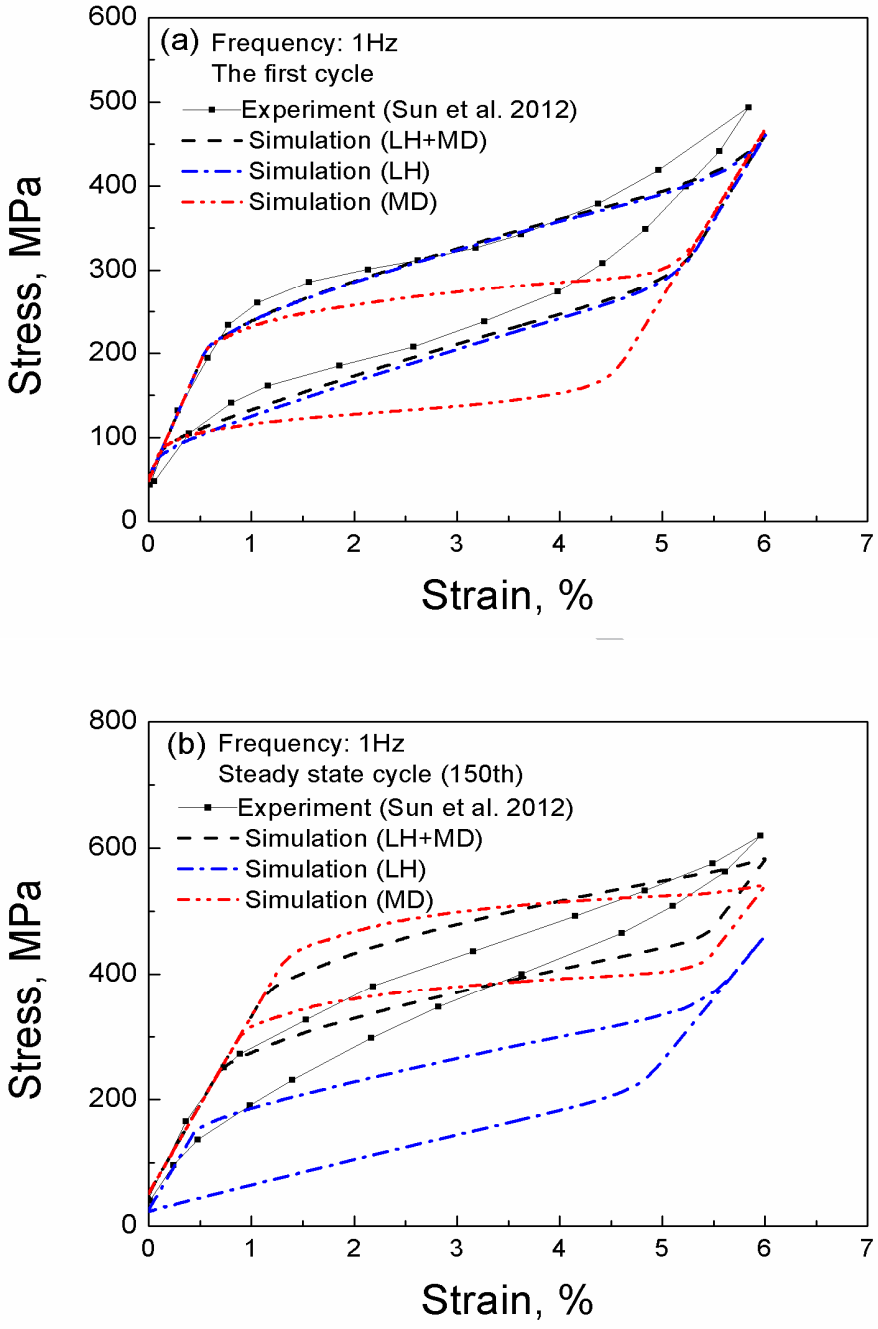

Fig. 12 Stress-strain curves at the loading frequency of 1Hz: (a) in the first cycle; (b) in the steady cycle (the 150th cycle).

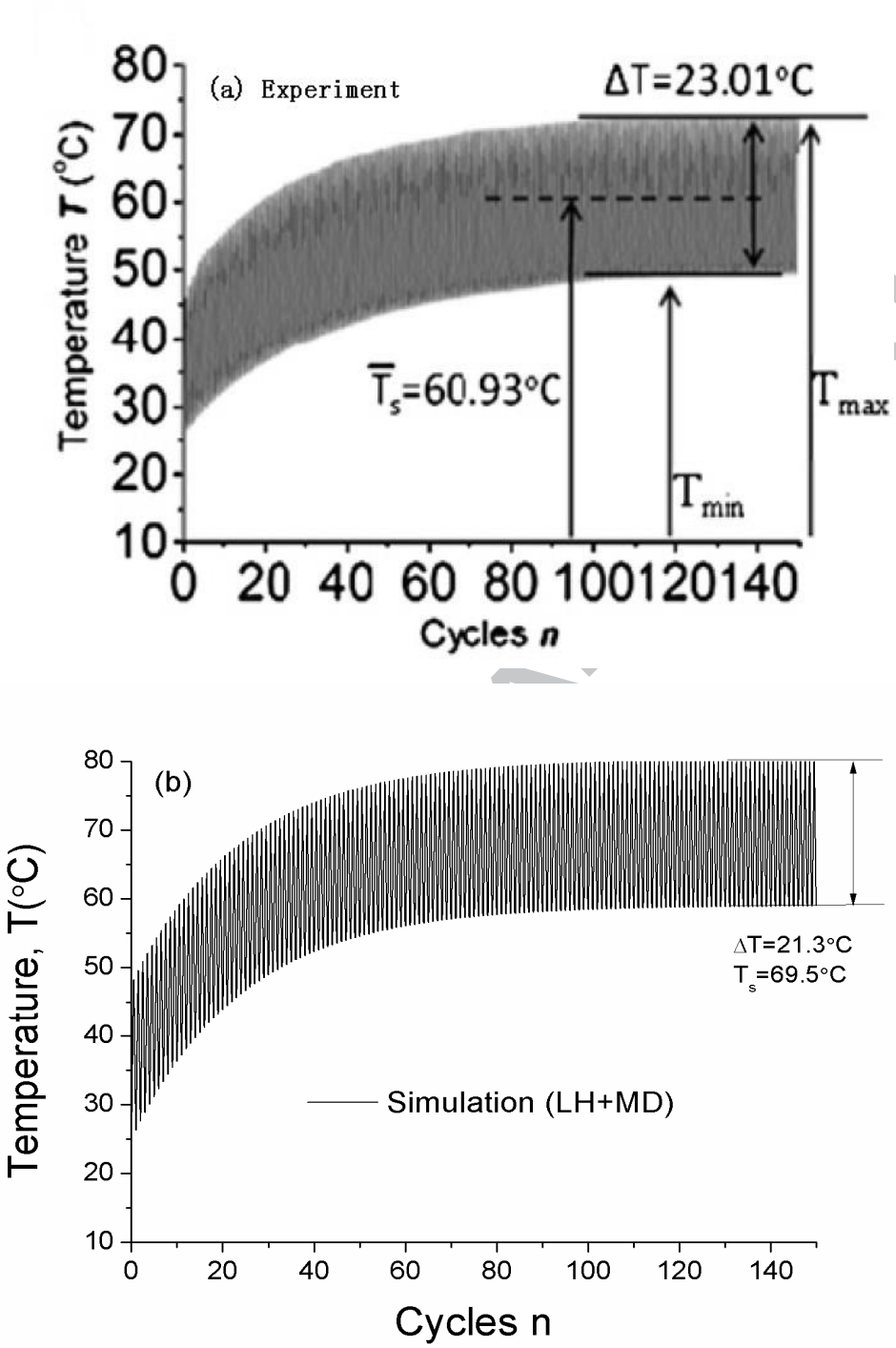

Fig. 13 Curves of temperature vs. cycles at the loading frequency of 1Hz: (a) experiment (from Sun et al., 2012); (b) simulation (LH+MD); (c) simulations (LH and MD separately).

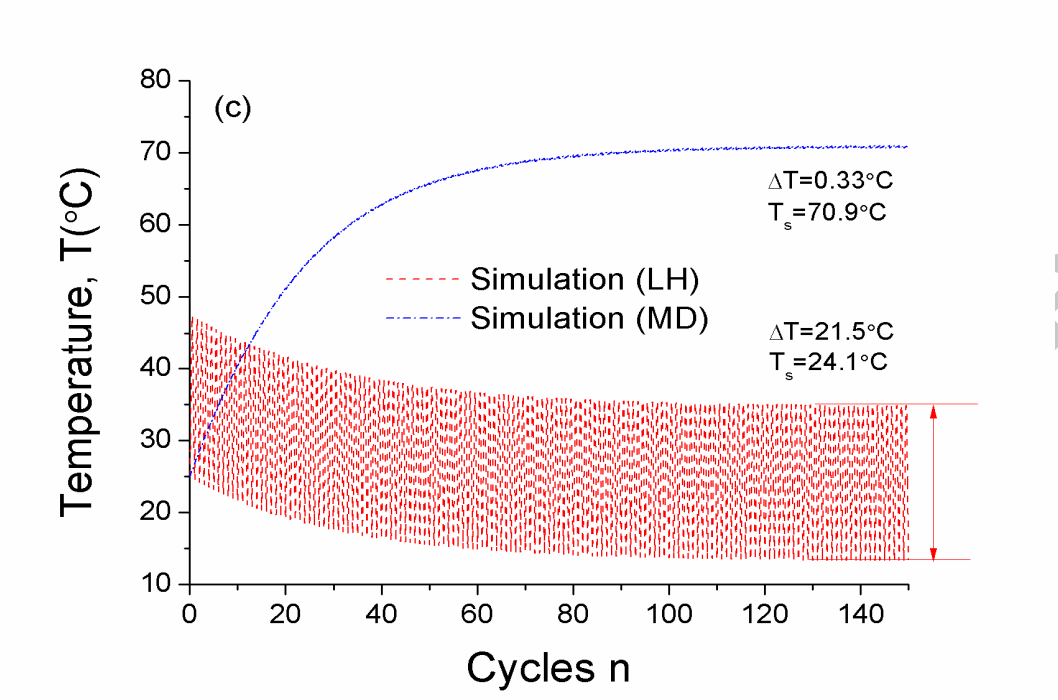

Fig. 13 (continued) Curves of temperature vs. cycles at the loading frequency of 1Hz: (a) experiment (from Sun et al., 2012); (b) simulation (LH+MD); (c) simulations (LH and MD separately).

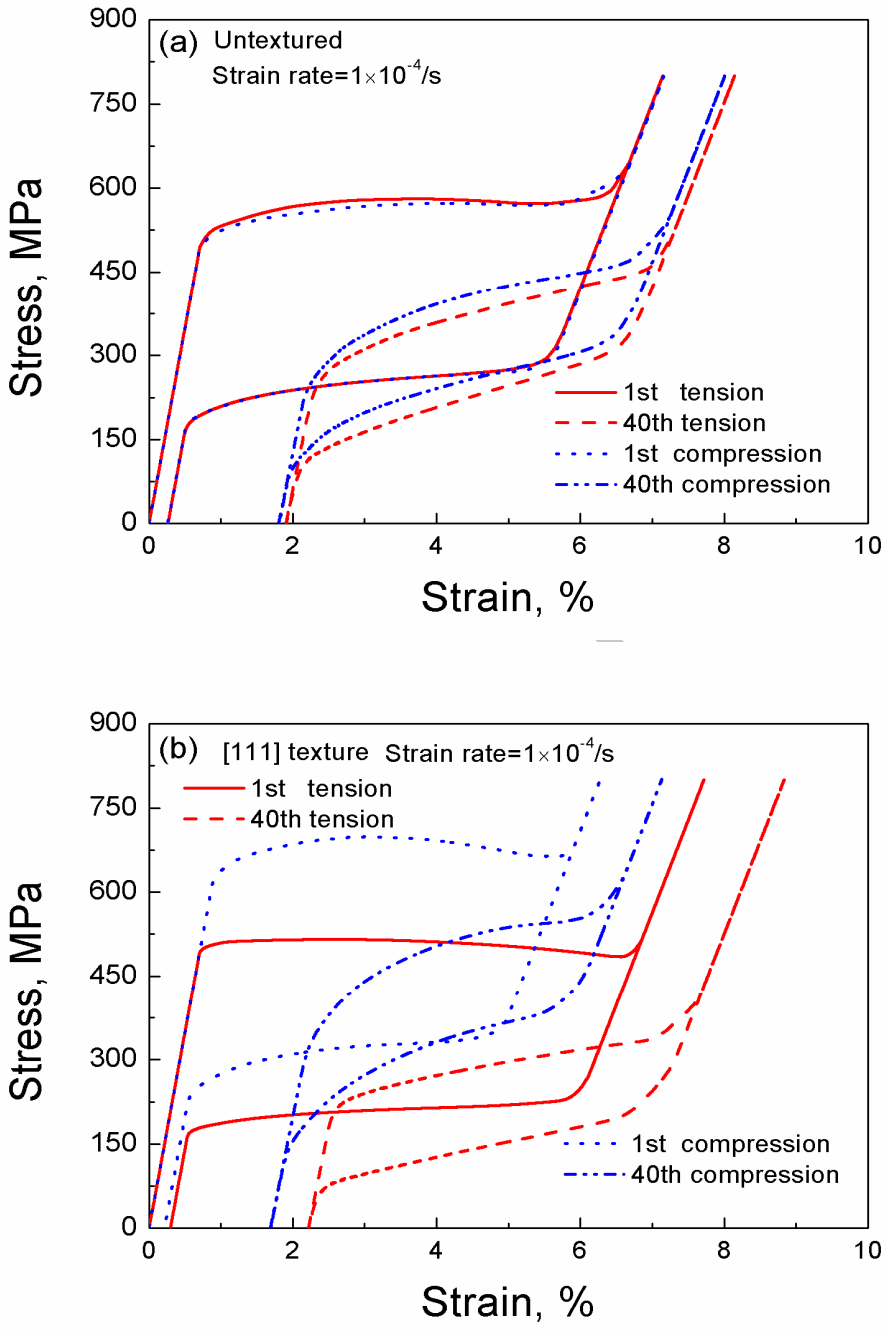

Fig. 14 Predicted stress-strain curves for the repeated tension-unloading and compression-unloading in the 1st and 40th cycles and at the strain rate of 1×10^{-4}/s: (a) un-textured polycrystalline aggregates; (b) polycrystalline aggregates with the [111]-type texture.

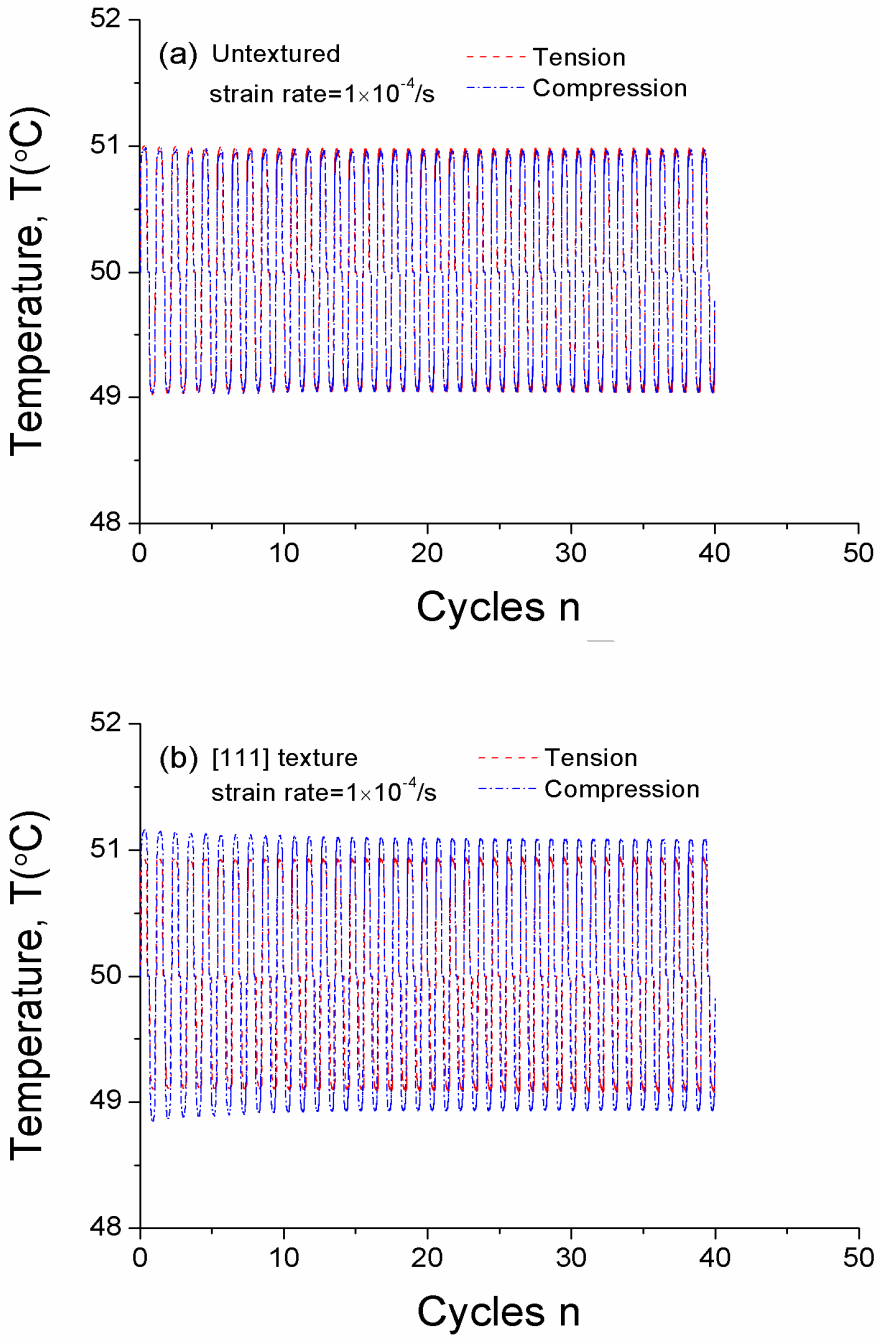

Fig. 15 Curves of temperature vs. cycles at the strain rate of 1×10^{-4}/s: (a) un-textured polycrystalline aggregates; (b) polycrystalline aggregates with the [111]-type texture.

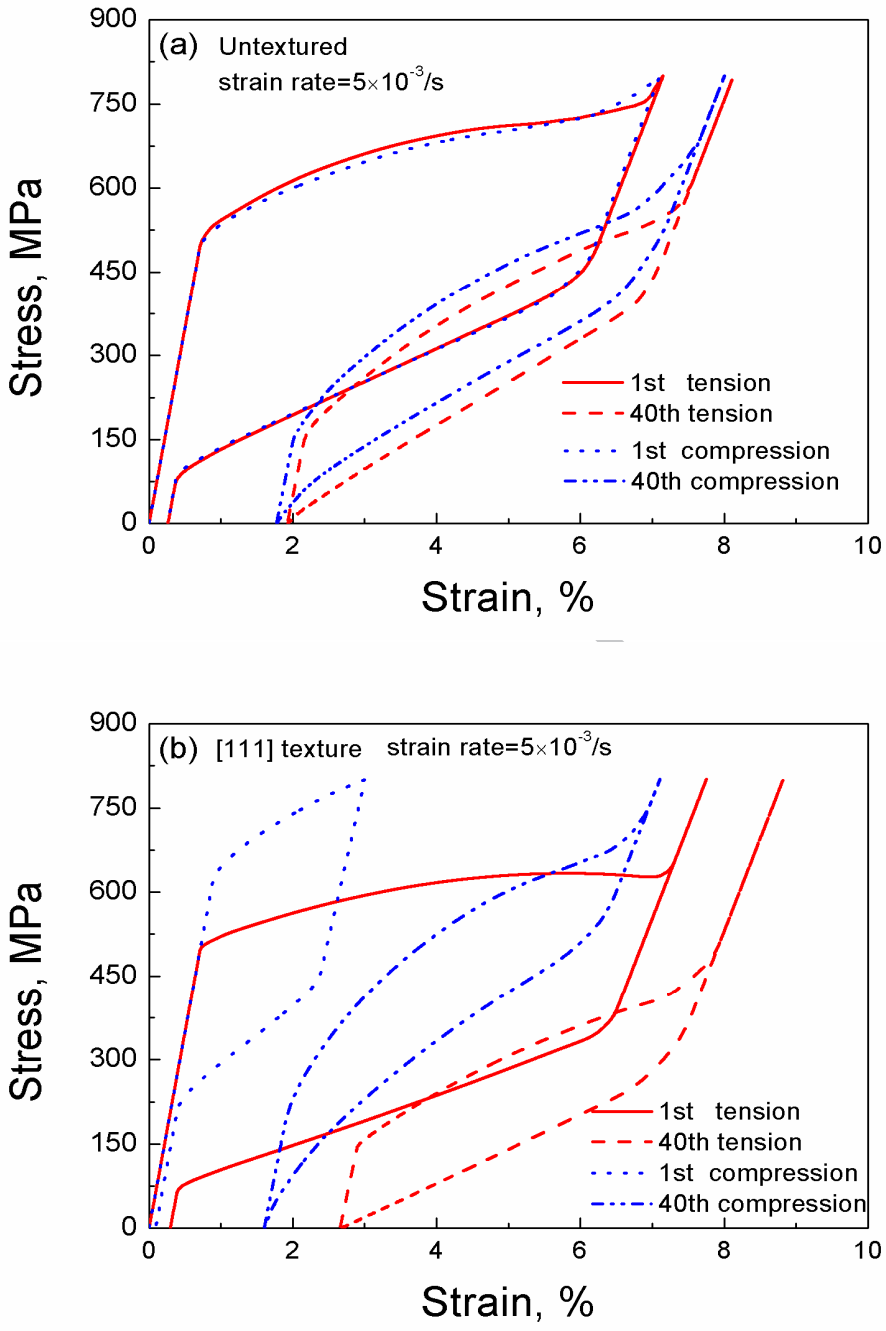

Fig. 16 Predicted stress-strain curves for the repeated tension-unloading and compression-unloading in the 1st and 40th cycles and at the strain rate of 5×10^{-3}/s: (a) un-textured polycrystalline aggregates; (b) polycrystalline aggregates with the [111]-type texture.

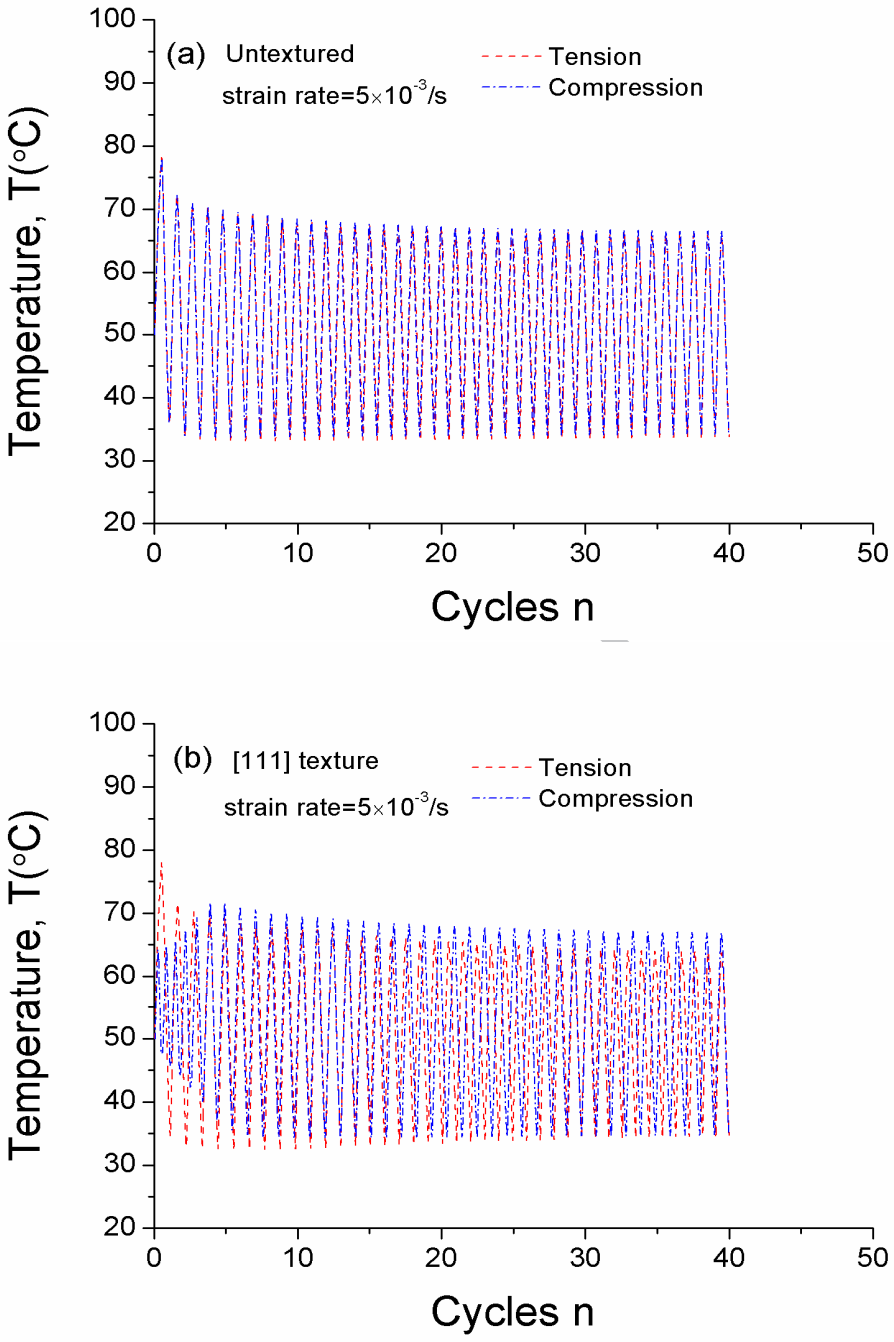

Fig. 17 Curves of temperature vs. cycles at the strain rate of 1×10^{-4}/s: (a) un-textured polycrystalline aggregates; (b) polycrystalline aggregates with the [111]-type texture.

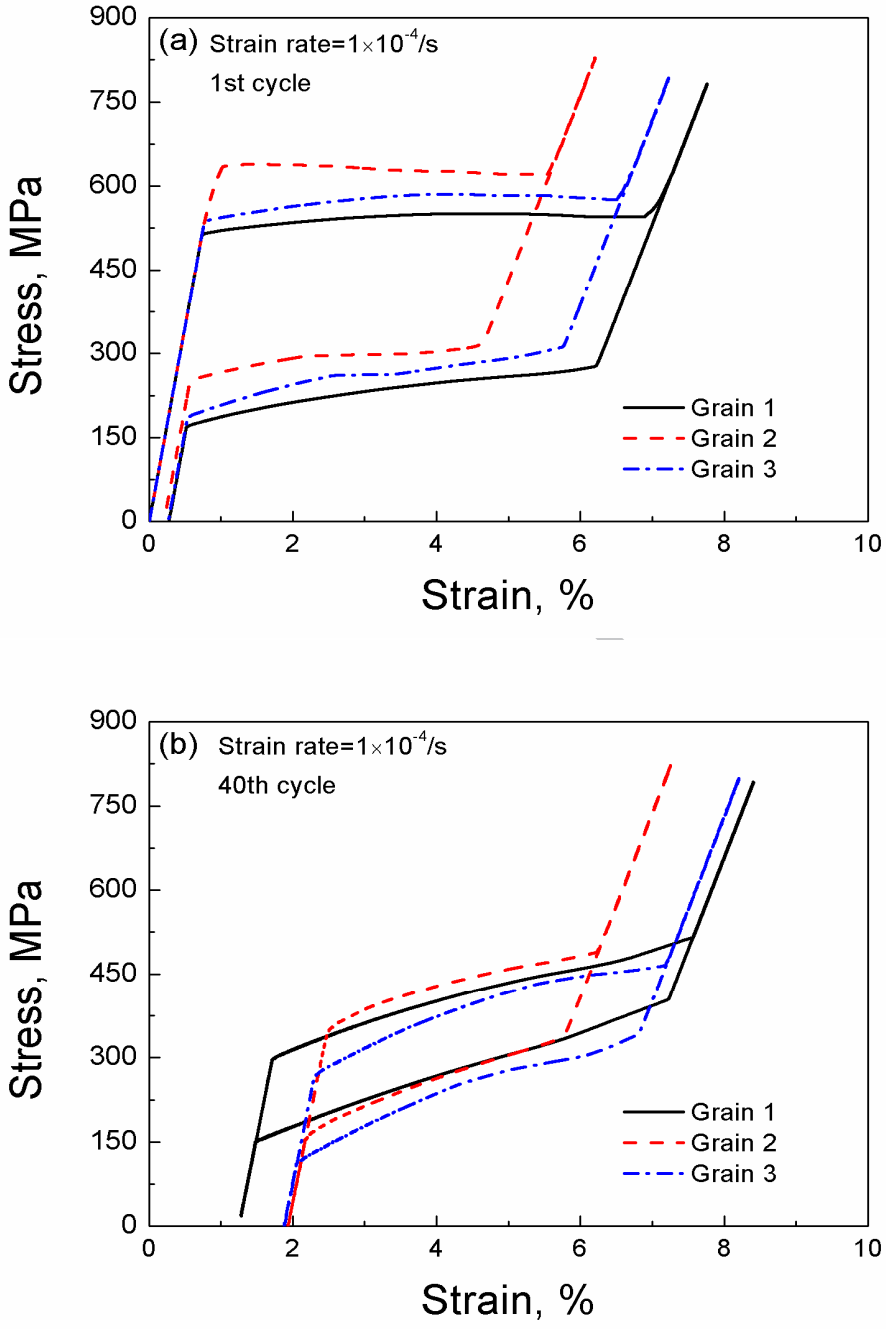

Fig. 18 Stress-strain curves of three chosen grains at the strain rate of 1×10^{-4}/s: (a) 1st cycle; (b) 40th cycle

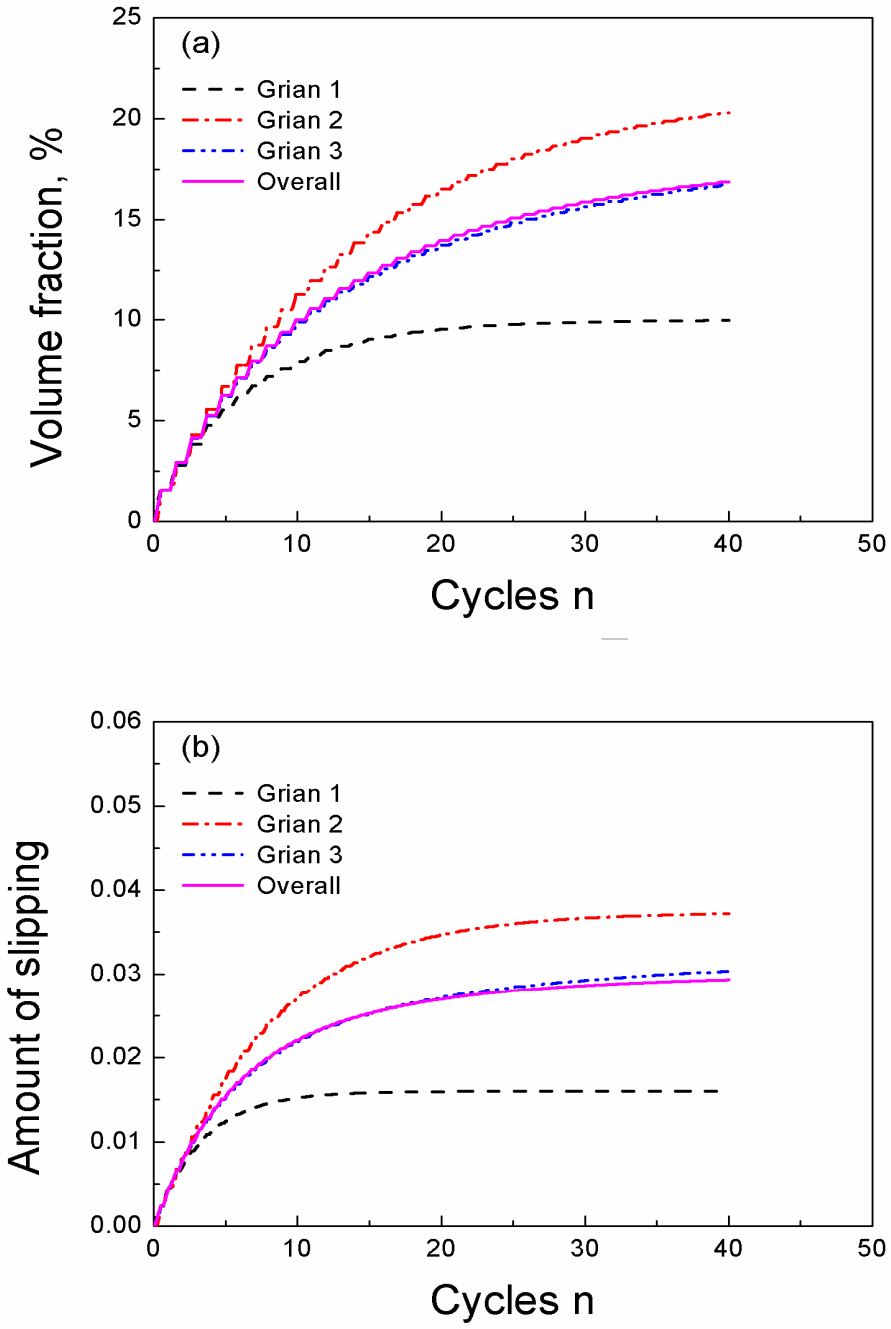

Fig. 19 Evolution curves of the overall responses and three chosen grains at the strain rate of 1×10^{-4}/s: (a) volume fraction of residual martensite; (b) Amount of friction slipping.

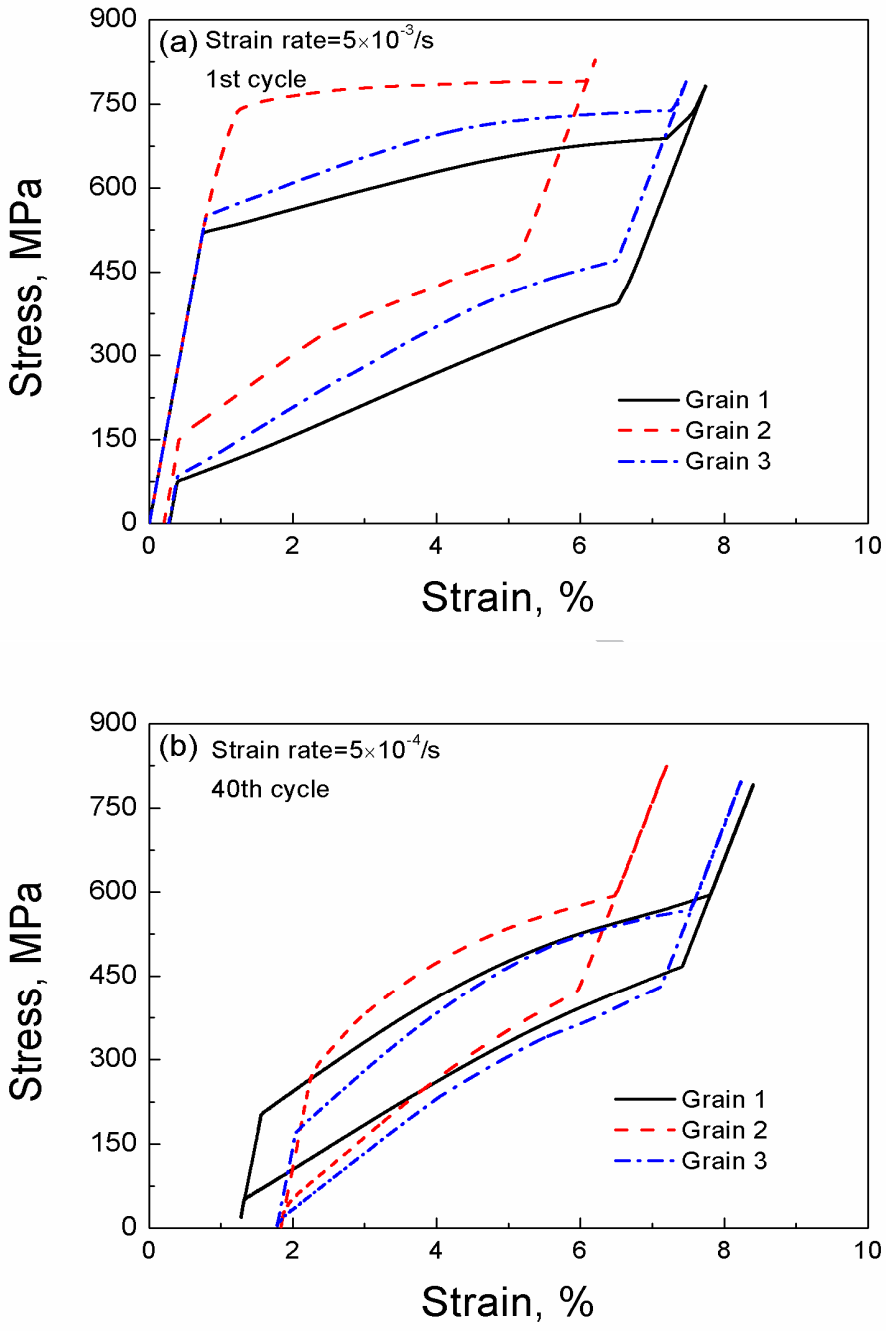

Fig. 20 Stress-strain curves of three chosen grains at the strain rate of 5×10^{-3}/s: (a) 1st cycle; (b) 40th cycle

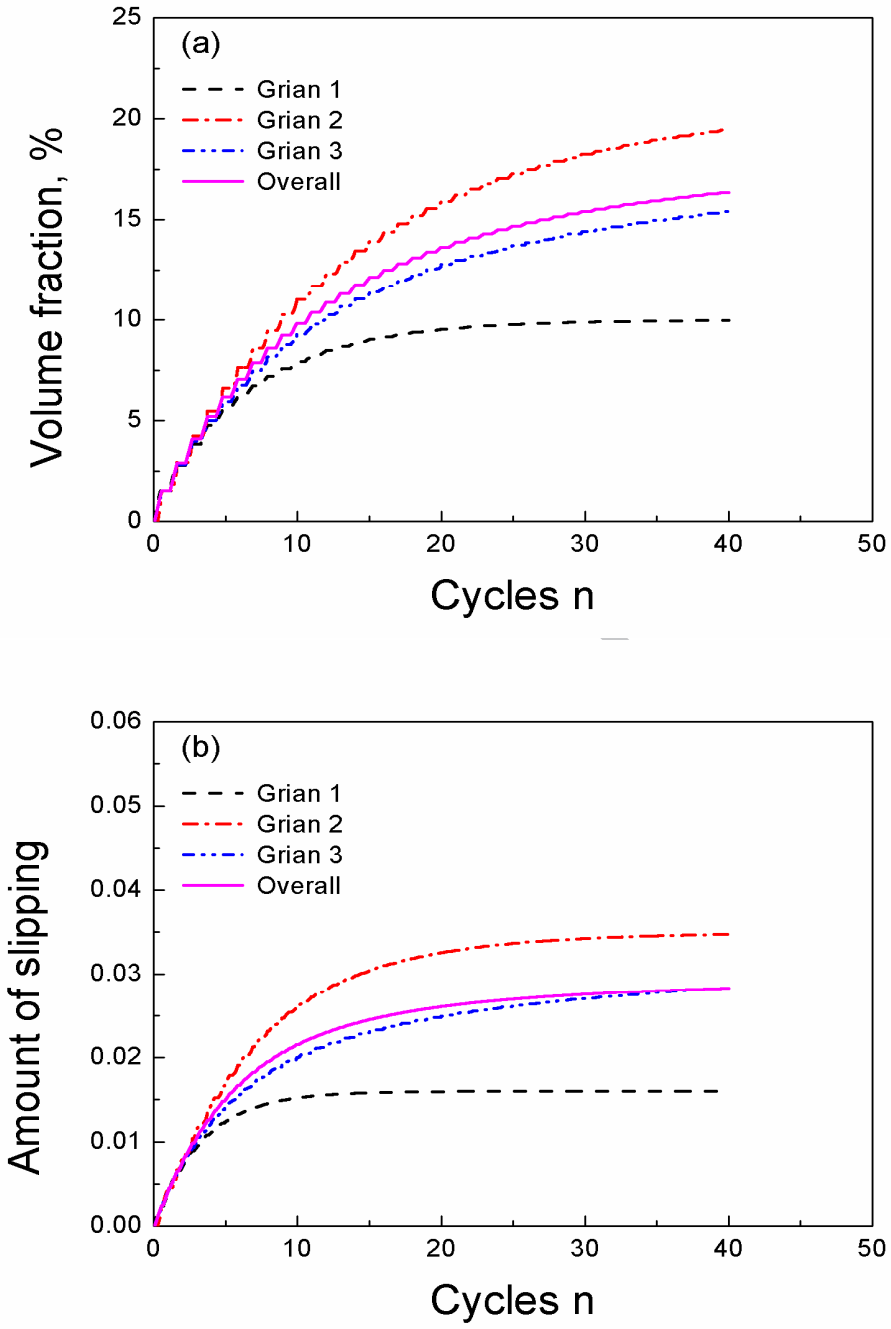

Fig. 21 Evolution curves of the overall responses and three chosen grains at the strain rate of 5×10^{-3}/s: (a) volume fraction of residual martensite; (b) Amount of friction slipping.

Research Highlights for the paper

(1) A crystal plasticity based constitutive model is constructed for the NiTi SMAs.

(2) Rate-dependent cyclic deformation of the NiTi SMA is reasonably described.

(3) Internal heat production during the cyclic deformation is considered.

(4) Temperature changes occurred during the cyclic deformation are predicted well.